Doctoral Dissertations

Student Theses and Dissertations

Fall 2021

Layer-to-Layer Feedback Control for Direct Energy Deposition Additive Manufacturing

Michelle Gegel
Missouri University of Science and Technology

LAYER-TO-LAYER FEEDBACK CONTROL FOR DIRECT ENERGY DEPOSITION

ADDITIVE MANUFACTURING

by

MICHELLE LEE GEGEL

A DISSERTATION

Presented to the Graduate Faculty of the

MISSOURI UNIVERSITY OF SCIENCE AND TECHNOLOGY

In Partial Fulfillment of the Requirements for the Degree

DOCTOR OF PHILOSOPHY

in

MECHANICAL ENGINEERING

2021

Approved by:

Douglas Bristow, Advisor
Robert Landers, Co-Advisor
Frank Liou
John Singler
Jagannathan Sarangapani
Sandipan Mishra

PUBLICATION DISSERTATION OPTION

This dissertation consists of the following three articles, formatted in the style used by the Missouri University of Science and Technology.

Paper I: Pages 4-42 are intended for submission to the Journal of Additive Manufacturing.

Paper II: Pages 43-64 are intended for submission to the International Journal of Mechatronics.

Paper III: Pages 65-86 are intended for submission to IEEE Transactions on Control System Technology.

ABSTRACT

Additive manufacturing (AM) has garnered much attention in recent years, some calling it the fourth industrial revolution. It was first used to create rapid prototypes, although recent efforts have been made to advance the technology towards production of functional parts. This requires advancement in the materials used in AM, as well as the ability to produce quality parts repeatably. More specifically, direct energy deposition (DED) of metal powders is a process capable of producing and repairing parts with complex geometries; however, it is not widely used in industry due to challenges with quality control. In this process, metal powder is dispensed from a nozzle and a laser beam melts the incident powder particles and a portion of the underlying surface. The melt pool is translated along the desired toolpath and parts are constructed in a layer-by-layer fashion. Several process inputs determine the deposition quality, including powder feed rate, laser power and nozzle speed. These inputs, as well as the environmental conditions, are subject to random fluctuations that can cause geometric defects during deposition. Such defects often propagate through to subsequent layers and are amplified, rendering the final part unusable. The objective of this work is to improve the geometric accuracy of parts produced by metal powder DED by designing and implementing process feedback control. The strategy involves measuring the part height after each layer and adjusting the nozzle speed trajectory for the next layer according to a designed control law. The major contributions of this work are 1. the construction of an open-architecture metal powder DED system that is capable of implementing layer-to-layer control and 2. the development of controllers to improve part morphology accuracy in metal powder DED.

ACKNOWLEDGMENTS

TABLE OF CONTENTS

SECTION

LIST OF ILLUSTRATIONS

Figure   Page

PAPER I

PAPER II

PAPER III

LIST OF TABLES

SECTION

1. INTRODUCTION

The burst of additive manufacturing (AM) technologies in recent decades has been called "Industry 4.0," characterized by the fusion of digital design with physical production. The ability to produce parts directly from digital models and without custom tooling or fixturing offers minimal lead time and flexibility for design changes. Furthermore, the nature of adding, rather than removing, material to create the desired part has the potential for minimal material waste. Although constructing objects in a layered-approach goes back to the making of topographical maps in the 1800's, the modern era of additive manufacturing can be marked by the invention of several additive systems in the 1980's and 1990's: stereolithography, fused deposition modeling and powder bed fusion [1]. Since then, additive technologies have expanded to a broad variety of materials - concrete, ceramic and even living tissue - and have grown from prototyping applications towards production of functional, serviceable parts.

Metal AM has received much attention by researchers because of its potential to create fully functional parts with desirable material properties, particularly for materials that are difficult to machine such as tungsten or cobalt alloys [2]. One type of metal AM process is wire-fed, where wire filament is fed into a melt pool formed by a high-power heat source such as a laser or electron beam. This process is extremely material efficient and is well-suited for large-scale applications, such as sparse aerospace parts. On the opposite end of the scale, are powder-bed processes, which have a feature resolution of 20 μm [3]. In powder-bed metal AM, the entire build footprint is encased by loose powder and the laser selectively sinters the loose powder to underlying features before spreading a thin layer of

loose powder on top and repeating. This process achieves surface finishes as good as 15 μm (R_a) [4], although wastes a significant amount of metal powder unless the un-sintered powder can be recycled.

The particular process studied in this dissertation is a blown-powder process known as Laser Metal Deposition (LMD), Direct Energy Deposition (DED) or Laser Engineered Net Shaping (LENS ®). In DED, metal powder is blown from a nozzle into a laser-formed melt pool and parts are constructed in a layer-by-layer fashion. Advantages of this type of metal AM include the ability to deposit on existing part geometries, which is useful for high-value part repair [5, 6], as well as the ability to create functionally-graded parts, where the material composition gradually changes throughout a part's geometry [7, 8].

This work focuses on the deposition morphology in DED, which is influenced by a number of factors. The deposition behavior depends on the user's choice of process parameters such as laser power, nozzle speed, powder feed rate, initial part stand-off distance and the vertical nozzle increment between layers. In addition, the melt pool shape is governed by complex thermal-physical dynamics, including surface tension forces and phase change, which are complex to model with high fidelity. The part as a whole also experiences heat accumulation and heat transfer dynamics throughout the process that are challenging to model accurately for arbitrary part geometries. Lastly, non-deterministic influences on the deposition morphology include fluctuations in the powder feed or convection from the part due to environmental conditions. Due to these factors, it is desirable to incorporate in-process sensing along with feedback control for DED.

Much research has been done to control various aspects of the DED process, typically involving melt pool characteristics such as length, width or temperature. In [9, 10, 11], laser power was adjusted to regulate the melt pool temperature. However, it was concluded that temperature control alone was not sufficient to produce quality deposition morphology. Nozzle speed was adjusted to achieve desired clad height in [12].

A significant phenomenon that existing work fails to account for is the propagation of morphology defects with layer. Most previous work focuses on measuring and responding to measurements in real-time and does not account for affects of previous layers on the current layer deposition. However, often a small defect occurs on some layer and then, with the addition of subsequent layers, the defect persists or amplifies, ultimately causing the part build to fail. Thus, the process dynamics should be considered in two dimensions: 1. within the layer and 2. layer-to-layer. A control-oriented modeling framework that accounts for layer-to-layer dynamics in DED was first introduced by Sammons in [13]. Furthermore, since the process dynamics evolve with layer, a layer-to-layer control strategy was proposed in [14] and also implemented in this dissertation work.

The layer-to-layer control strategies developed in this dissertation were implemented on a custom-built and open-architecture DED machine. The system includes a laser line scanner that acquires measurements of the part height in between layers. After depositing and measuring each layer, the control algorithm uses the measurements to generate the nozzle speed trajectory for the next layer in order to correct for height errors measured on the previous layer.

This dissertation presents three papers which are in preparation for publication. The first paper focuses on the measurement instrument used for feedback in this work - the laser line scanner. The accuracy and repeatability errors inherent to this measurement devices are characterized and quantified. The second paper develops norm-optimal control for a repetitive process model. Although norm-optimal control is widely used, it has not been previously extended to a repetitive process. The control algorithm was implemented on thin wall parts with constant layer thickness. In the third paper, the control formulation is extended to the case of parts that have varying layer thickness. A novel 2D loop-shaping design is presented and demonstrated for a 5-axis part. The papers are followed by a conclusions section.

PAPER

I. EVALUATION OF A LASER LINE SCANNER FOR LAYER-BY-LAYER MEASUREMENT IN LASER METAL DEPOSITION

Michelle L. Gegel
Department of Mechanical & Aerospace Engineering
Missouri University of Science and Technology
Rolla, Missouri 65409–0050

Adam Nisbett
Department of Mechanical & Aerospace Engineering
Missouri University of Science and Technology
Rolla, Missouri 65409–0050

Douglas A. Bristow
Department of Mechanical & Aerospace Engineering
Missouri University of Science and Technology
Rolla, Missouri 65409–0050
Tel: 573–341–6559
Email: dbristow@mst.edu

Robert G. Landers
Department of Aerospace & Mechanical Engineering
University of Notre Dame
Email: rlanders@nd.edu

ABSTRACT

This work evaluates laser line scanning as a technique for in-process measurement of parts manufactured via Laser Metal Deposition (LMD). Laser line scanners provide a convenient means of rapidly acquiring geometric measurements of the part between layers, which generates information that can be used either to take corrective action during a part build or to qualify the part post process. However, care is needed in properly

understanding scanner inaccuracies and digital image artifacts that may lead to incorrect actions. First, a method of identifying and correcting errors due to installation misalignment is presented, which can be performed for any commercially available line scanner device. Then, sources of measurement error are described in detail, including orientation of the scanner with respect to the part and discontinuities in the part texture or features. While many in the literature affirm the existence of such errors, this work seeks to quantify the errors, specifically in application to measuring LMD parts. Experiments were performed to characterize the repeatability and accuracy errors for a representative laser scanner. Scanning in a direction perpendicular to the cladding was found to produce the greatest number of invalid data points, six times more than the other orientations, although the remaining valid data points had the smallest standard deviation, 4.6 μm as opposed to 5.8 μm and 8.5 μm for the other orientations. Measurements of LMD features and surface roughness were compared against traditional non-optical devices, namely a coordinate measuring machine and contact-style profilometer. The scanner was found to measure surface roughness accurately within the variation of the roughness parameters throughout the cladding sample. Finally, the use of build history in rejecting parts with internal defects was demonstrated on a part built with layer-by-layer scanning.

Keywords: laser line scanning, laser triangulation, laser metal deposition

1. INTRODUCTION

In-process sensing and controls are high-priority objectives for advancing additive manufacturing (AM) technologies, as recognized by NIST and the research community [1, 2, 3, 4]. Sensing is needed to "find defects and processing issues early in the process" [2]. Often when geometric abnormalities develop early in the build process, the defects propagate throughout the build until they become significant enough to render the final part

unusable. By detecting geometric defects as they arise, a build system would be able to recover the part, through modified nozzle paths or other remedies, or else abort the part before additional time and material are wasted.

An attractive technique for in-process monitoring of part geometry is laser line scanning. This method obtains dense measurements quickly and, because it uses active illumination, is robust to lighting conditions in the environment. Also, the amount of time required to scan a given area can be adjusted by changing the speed at which measurements are acquired. This changes the measurement resolution, but can be adjusted without physically repositioning the measurement device, which provides flexibility in optimizing the trade-off between scan time and resolution.

Here, laser line scanning will be evaluated for the process known as Laser Metal Deposition (LMD), in which powdered metal is blown into a melt pool formed by a laser and parts are built in a layer-by-layer fashion. In LMD, part quality is highly dependent on process inputs, including stand-off distance, laser power, powder flow rate and print speed, and also on process conditions which may change throughout the course of a build, such as the rate of heat transfer from the part and the melt pool temperature. Fluctuations in these inputs and conditions as well as height variations of previous layers can result in height variations in layer thicknesses. In-situ height sensing for LMD would be able to detect these variations in layer thickness, which would be useful for in-process correction, as well as for post-process qualification.

In the literature, several types of cameras, including CCD, CMOS and IR, have been used to measure melt pool geometry in-situ. In some cases the cameras were aligned coaxially with the deposition head, while in other cases the cameras viewed the melt pool at an angle. Coaxially aligned IR cameras were employed in [5, 6] to measure melt pool area, while a triangular arrangement of three CCD cameras was used in [7, 8] to obtain melt pool height. These are cases of passive illumination, in which cameras rely on ambient light conditions. In what is known as active illumination, cameras are used in conjunction

with light sources and optical filters to isolate the wavelength of interest and reject radiation generated by the process itself. In [9], UV light emitting diodes were directed at the processing zone to provide a clearer image for a CMOS camera which was equipped with a band-pass filter to permit the passage of UV wavelengths.

Laser scanning is a form of active illumination in which a laser spot or line is projected onto the surface and viewed at an angle by a camera. There are a few instances in previous work of laser scanning being used for LMD part inspection. In [10, 11], laser scanning was employed to measure depositions post-process. A spot displacement sensor was incorporated in closed-loop height control of LMD in [12] and a line scanner was used in [13, 14]. There are other instances of laser scanners being used in similar manufacturing processes, namely wire-fed laser AM, gas metal arc welding (GMAW) and large-scale polymer AM. For the GMAW process in [15], a line scanner was positioned to trail the processing zone and obtain bead width and height measurements during deposition. In [16], a laser line scanner acquired height measurements between layers of a wire-fed AM process for closed-loop height control. Although the controlled builds demonstrated improved dimensional accuracy over the open-loop builds, the authors mentioned difficulties with obtaining reliable part scans and indicated that knowledge of scanner uncertainty would be useful in controller design and performance evaluation. Laser line scanning was also used for large-scale polymer AM in [17]. Although polymers are typically less reflective than metal surfaces, these authors also mentioned the presence of outlier data points and expressed a need to investigate the error characteristics of the scanner.

The error characteristics of scanner data are highly dependent on the optical properties of the surface. Stavroulakis and Leach [18] indicate that the surface roughness of AM parts can actually be beneficial in breaking up specular reflections; however, if the optical roughness becomes too large, i.e., the feature height is comparable to a quarter of the wavelength, it can increase speckle noise uncertainties. Wang and Feng [19] used gauge blocks with highly reflective surfaces to investigate the effect of the part geometry and

incident angle on outlier frequency. They found that outliers were reduced by increasing the angle of incidence between the scan beam and surface normal. However, with curved surfaces this proves to be impossible and there remain outlier points when using any single scan direction. Using multiple passes with different scan angles was shown to allow for the identification and removal of outlier points.

Various error compensation methods for laser scanning have been proposed. Isheil et al. [20] created a compensation model based on scan depth and incidence angles. Abbasinejad et al. [21] show that systematic error around sharp height discontinuities has a strong correlation with edge orientation with respect to the scan direction. To correct for this error, they combine multiple scans taken at different orientations and weight the data for sharp edges depending on the scan orientation. Other studies have proposed solutions which rely on intensity data from the original images from which the measurement data is extracted. Although effective, these methods can be computationally expensive and commercially available laser scanners may not provide access to the original images. Reiner and Stankiewicz [22] assume that the nominal part geometry is known and that the dimensional and transformational parameters are unknown. They iteratively compute estimated locations for the imaged scan lines based on the current modeled geometry, filter out reflections which fail to fit the model, and then recompute the model parameters. Curless and Levoy [23] demonstrate that rather than simply evaluating each line image to determine the central brightness, it is more beneficial to use a spacetime computation based on the contribution of the illumination of any given point on the part to the corresponding imaged points over sequential images to reduce the errors due to shape discontinuities in the part.

Knowledge of the noise and error contained in line scanner measurements is relevant for feedback control applications, where the measurements are used to determine corrective action. Although the literature is rich with studies on various aspects of laser line scanning, its suitability for measuring LMD surfaces has not been well-studied. This work investigates the use of a laser line scanner as a measurement instrument for in-process sensing for LMD

and seeks to characterize the accuracy and repeatability in measuring LMD parts. Section 2 describes how a laser line scanner operates and details the hardware used in this work. A procedure for aligning the laser scanner to the motion system is presented in Section 3, which can be applied even to devices that do not allow the user access camera images. Section 4 provides experimentally obtained results for repeatability in measuring LMD surfaces while Section 5 addresses accuracy in measuring LMD features, identifying individual beads, and quantifying surface roughness. A demonstration of layer-by-layer scanning during a part build is given in Section 6, which illustrates how in-process scanning can be used to obtain knowledge of internal defects.

2. LASER LINE SCANNER FUNDAMENTALS

This section provides an overview of laser line scanner operation and sources of measurement error. The main components of a laser line scanner are illustrated in Figure 1. A half-cylindrical lens spreads a laser beam into a line which is projected onto the part. The projected laser line is then imaged by a camera situated at a known distance and orientation from the laser source. Since the geometry relating the illuminated surface and the image frame is triangular, the measurement technique is often referred to as "laser triangulation" [18]. From each camera image, a height profile is extracted that represents the part height along the laser stripe. By traversing the stripe across the part and acquiring profiles at designated intervals, a 3D scan is obtained. Measurement errors fall into two main categories: invalid data and distorted measurements. Sources of invalid data include specular reflections, which are particularly problematic for highly reflective surfaces, and occlusions. Distorted measurements of valid points can be due either to errors in the device model or to discontinuities in the measured surface. These error types will be discussed in more detail below.
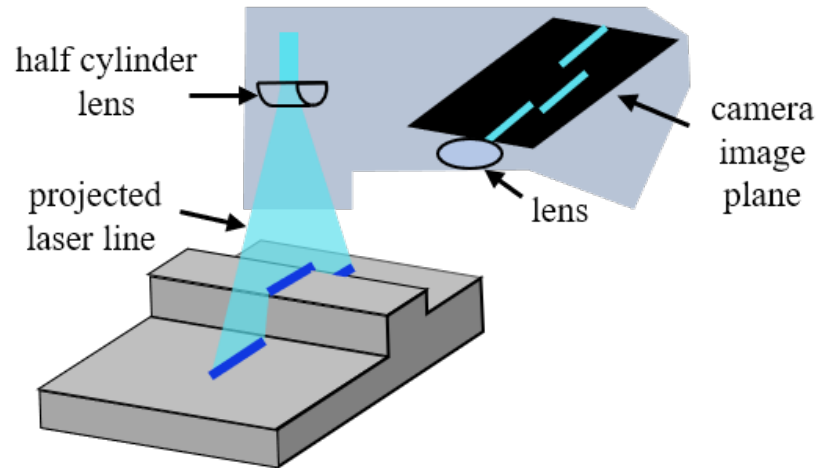
Figure 1. Diagram of a laser line scanner.

2.1. INVALID MEASUREMENTS

Specular reflections occur when the beam is reflected from the surface at an angle equal to the incident angle. By contrast, diffuse reflections scatter light in all directions and so can be observed from any angle. The proportion of light that is reflected specularly versus diffusely depends on the surface. Figure 2 illustrates an example of a specular reflection causing invalid data. Here, a specular reflection strikes another portion of the part surface, creating a secondary diffuse reflection that is visible in the image frame. If the secondary reflection is used in the height calculation, the measurement will be inaccurate because the calculation assumes that the reflection originates from a location coincident with the laser beam. There are multiple approaches to handling errors due to secondary reflections. One option is to select the brightest reflection, which will often correspond to the primary diffuse reflection since light loses some of its intensity with each redirection. Alternatively, since secondary reflections often have wider intensity distributions than primary reflections, filtering based on these distributions may serve to eliminate false data. For a very reflective surface, however, specular reflections retain a large portion of the intensity such that the secondary diffuse reflections may have comparable intensity as the primary. In addition, if the specular reflection happens to be directed towards the camera, then it can appear
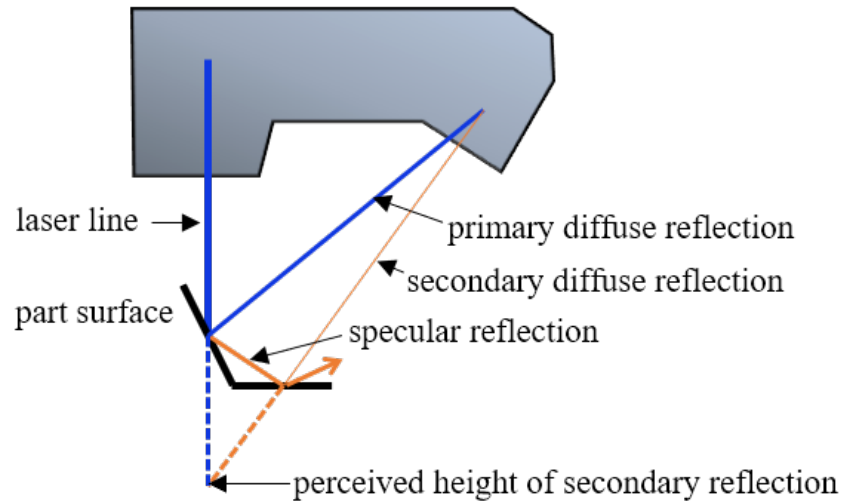
Figure 2. Diagram of a specular reflection.

much brighter than the initial diffuse reflection. Another option is to select the reflection with the highest or lowest apparent surface height if the errors are known to be skewed in a particular direction. Some scanners also have the ability to project light polarized in perpendicular directions. Since light becomes partially depolarized upon reflection, selecting the stripe with the least difference in polarization in the horizontal or vertical direction can successfully reject the secondary reflection. Lastly, an invalid data point can simply be recorded anytime multiple reflections are detected.

For parts with height discontinuities or complex geometries, occlusions can lead to missing data. Figure 3 shows an example of both camera occlusion, in which the line of sight between the camera and projected laser stripe is blocked, and laser occlusion, in which the surface is blocked from illumination. In general, camera occlusions will occur for edges running parallel to the laser stripe, while laser occlusion will occur for edges running perpendicular to the laser stripe. Occlusions of particular regions can be avoided by changing the part orientation with respect to the scan.

surface not visible to camera
due to occlusion

surface not lit by laser
line due to occlusion
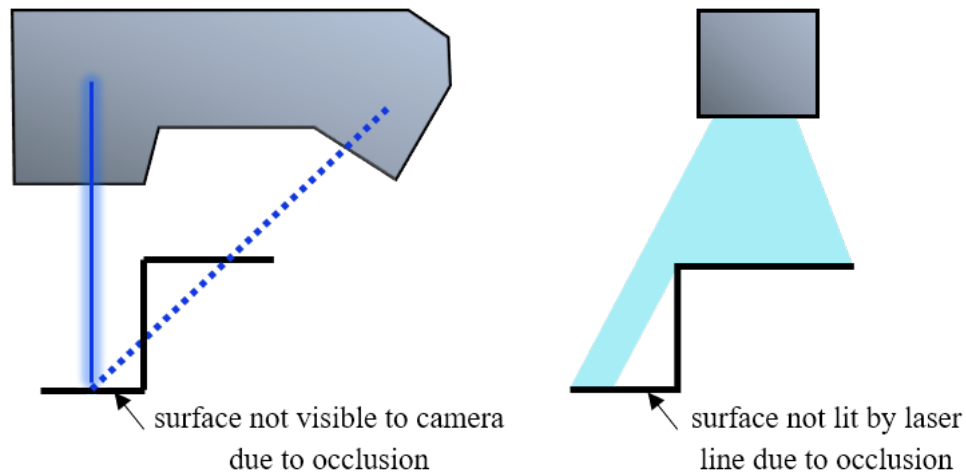
Figure 3. Diagram of occlusions.

2.2. DISTORTED MEASUREMENTS

Distorted measurements arise from the fact that the projected laser beam has a Gaussian intensity distribution across its thickness. When measuring a flat and homogeneous surface, the centroid of the imaged intensity curve corresponds to the center of the beam. However, if the part has reflectance or shape discontinuities, the results will be skewed. Several examples are shown in Figure 4, where the laser beam width is intentionally exaggerated. Figure 4(a) shows the measurement of a flat homogeneous surface in which the centroid of the imaged intensity curve corresponds to the actual surface height. In Figure 4(b) there is a discontinuity in reflectivity, which could stem from either color or surface texture changes. In this case the centroid of the intensity curve will be skewed toward the more reflective surface and therefore the apparent surface height will be incorrect. Figure 4(c) depicts a height discontinuity that prevents a portion of the beam from reaching the camera; therefore, the centroid of the intensity curve will be shifted away from the missing surface. Figure 4(d) shows a height discontinuity in the opposite direction. In this case, although none of the laser beam is hidden, it is illuminating two different surface heights such that the centroid of the intensity profile will lie in between the two heights. For both

(a) Homogeneous flat surface.

(b) Reflectance discontinuity.

(c) Shape discontinuity.

(d) Shape discontinuity.
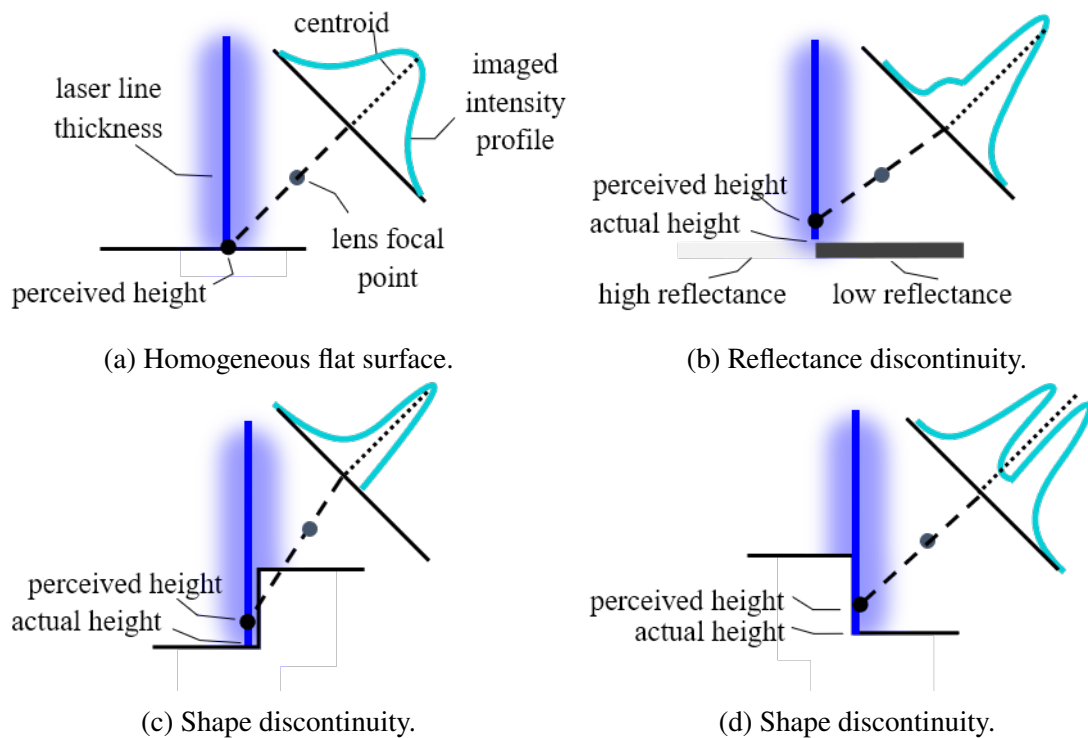
Figure 4. Types of surface discontinuities.

cases of height discontinuities, the measurement error will tend to smooth discontinuities found in the actual part. In addition to errors due to a split or absent portion of a Gaussian profile, rounded surfaces can result in measurement distortion [24], since surfaces reflect less light as they become perpendicular to the laser beam. In addition to surface discontinuities, speckle noise can cause shifts in the intensity distribution. Speckle noise, a natural phenomenon for coherent light, is when light waves share the same frequency and direction of propagation, but have random phases and amplitudes. While it is not possible to predict the actual error for any given measurement due to speckle noise, the error distribution has been well studied and modeled [18, 25].

Additional error sources for laser triangulation scanning also arise from the following factors. The focus of the laser line varies with distance, which causes errors for measurements at the lower limit of the measurement range. Positioning errors of the device with respect to the motion stages, as well as vibrations from the system motion during scanning, can also produce measurement errors.

2.3. HARDWARE DESCRIPTION

The line scanner used for this work was a Keyence LJ-V7200. The scanner has a height measurement range of 96 mm. The measurement range along the scan stripe varies from 51-73 mm over the height range. The resolution along the scan stripe is fixed at 100 μm, while the resolution in the scan direction is user-specified. In this work, image acquisition was triggered by the x-axis encoder of the LMD machine and thus the resolution in the scan direction was a user-specified multiple of the encoder resolution, which was 0.25 μm. This ensured evenly-spaced samples and a direct correlation between the axis position and a particular profile measurement. The factory defaults were used for the imaging settings, which included selection of the brightest reflection when multiple reflections were detected, as described previously. The option to interpolate across invalid data points was disabled and no profile filtering was used.

The LMD system consisted of a 5-axis CNC machine equipped with an Optomec LENS® Print Engine (LPE), see Figure 6. The system included an Optomec powder feeder and a 1 kW fiber laser (IPG YRL-1000-MM). These components, along with the axes motors, were connected to a National Instruments PXI system for centralized, open-source control. This allowed for flexibility in controlling the main process parameters of laser power, powder feed rate, and scan velocity.
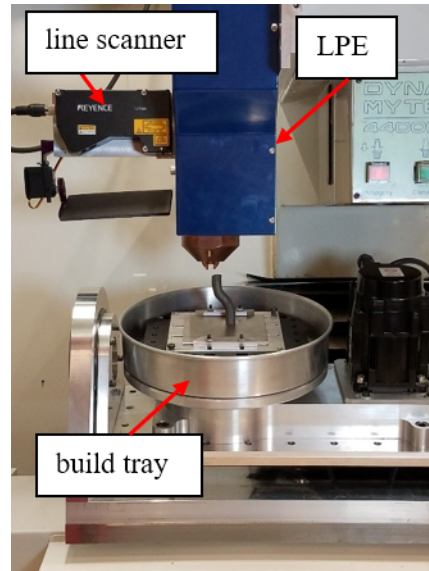
Figure 5. Laser line scanner mounted to LMD print head.
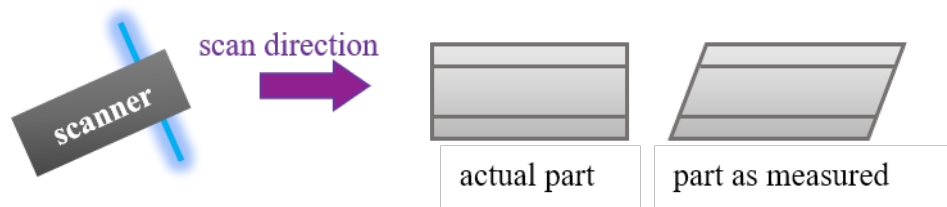
Figure 6. Diagram of measurement distortion due to scanner misalignment.

3. SCANNER ALIGNMENT PROCEDURE

During a scan, the scanner remains fixed while the part translates with the x-axis of the machine. If there is misalignment between the scanner and the machine axes, the measurements will be distorted as shown in Figure 6. Here, a method of identifying the misalignment between the scanner and motion axes is presented. Since this method does not require access to the raw images from the camera, it is applicable to any commercially available laser scanner device. First, the geometric relationship between the scanner and machine is modeled and then the model parameters are determined from experimental data. In order to relate points in the machine frame to points in the scan images, coordinate frames are established as shown in Figure 7. The work frame, denoted by the subscript w, is fixed
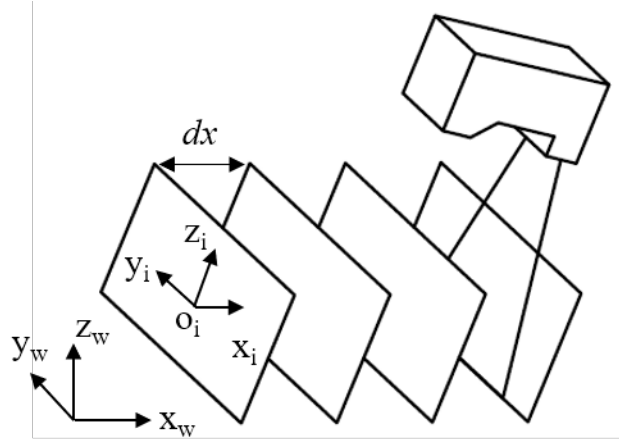
Figure 7. Coordinate frame designations.

and aligned with the machine motion axes. The image frame, denoted by the subscript i, shares the x axis orientation with the work frame, although the y_i and z_i axes are allowed to arbitrary orientation with respect to the x_i axis. A single point in the image frame can be mapped to the work frame by

$$p^w = R_i^w p^i + o_i^w$$

$$
\begin{bmatrix} p_x^w \\ p_y^w \\ p_z^w \end{bmatrix} =
\begin{bmatrix} 1 & r_{12} & r_{13} \\ 0 & r_{22} & r_{23} \\ 0 & r_{32} & r_{33} \end{bmatrix}
\begin{bmatrix} p_x^i \\ p_y^i \\ p_z^i \end{bmatrix} +
\begin{bmatrix} o_{ix}^w \\ o_{iy}^w \\ o_{iz}^w \end{bmatrix},
\tag{1}
$$

where p^w is the point expressed in the work frame, p^i is the point expressed in the image frame, R_i^w is the rotation transformation between the work and image frames and o_i^w is the translational offset between the work and image frames. Note that p_{yi} is the point's location along the scan stripe and p_{zi} is the height measured at that location. Although y_i and z_i are not necessarily orthogonal to x_i, they are constrained to be orthogonal with respect to each

(a)   (b)
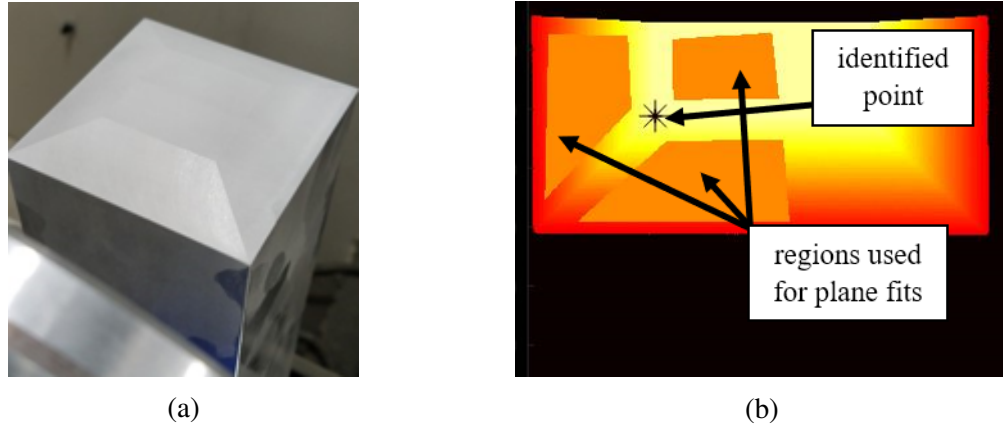
Figure 8. Photo, (a), and scan image, (b), of calibration part.

other as viewed in the work frame. This leads to the constraint equation

$$
\begin{bmatrix} r_{12} \\ r_{22} \\ r_{32} \end{bmatrix} \cdot \begin{bmatrix} r_{13} \\ r_{23} \\ r_{33} \end{bmatrix} = r_{12}r_{13} + r_{22}r_{23} + r_{32}r_{33}. \tag{2}
$$

The parameters of the rotation matrix R_i^w were determined experimentally by tracking a point with the scanner as it shifted along the y_w and z_w axes. The experiment utilized the calibration part shown in Figure 8(a), which was machined from aluminum and coated with an anti-reflective spray in order to minimize specular reflections. The part has four beveled surfaces such that the intersection of any three adjacent surfaces constitutes an easily identifiable point. Figure 8(b) shows a scan of the calibration part and the three regions selected for plane fits, along with the identified intersection point. To completely determine the rotation matrix R_i^w, a point on the calibration part must be scanned at a minimum of three locations. Equations will first be derived for the case where the calibration part is scanned at the minimum number of locations. The method is then extended to include several locations in order to mitigate the effects of measurement noise. Consider scanning the calibration part at two locations within the work frame, separated by a known distance,

ΔY, along the y_w axis. Although the calibration part is in different locations for each scan, the motion of the scanner with respect to the work frame is identical for both scans. The point in the first location is described by

$$p_1^w = \begin{bmatrix} p_{1x}^w \\ p_{1y}^w \\ p_{1z}^w \end{bmatrix} = R_i^w \begin{bmatrix} p_{1x}^i \\ p_{1y}^i \\ p_{1z}^i \end{bmatrix} + \begin{bmatrix} o_{ix}^w \\ o_{iy}^w \\ o_{iz}^w \end{bmatrix}. \tag{3}$$

Similarly, the point in the second location is described by

$$p_2^w = \begin{bmatrix} p_{2x}^w \\ p_{2y}^w \\ p_{2z}^w \end{bmatrix} = R_i^w \begin{bmatrix} p_{2x}^i \\ p_{2y}^i \\ p_{2z}^i \end{bmatrix} + \begin{bmatrix} o_{ix}^w \\ o_{iy}^w \\ o_{iz}^w \end{bmatrix}. \tag{4}$$

Then from equations (3) and (4), the following can be obtained

$$p_2^w - p_1^w = \begin{bmatrix} 0 \\ \Delta Y \\ 0 \end{bmatrix} = R_i^w \begin{bmatrix} \Delta u_x^i \\ \Delta u_y^i \\ \Delta u_z^i \end{bmatrix} \tag{5}$$

where

$$\Delta u_x^i = p_{2x}^i - p_{1x}^i$$

$$\Delta u_y^i = p_{2y}^i - p_{1y}^i$$

$$\Delta u_z^i = p_{2z}^i - p_{1z}^i \tag{6}$$

Note that ΔY is the commanded shift in y_w, which is known, and Δu_x^i, Δu_y^i and Δu_z^i are the coordinates of the point as it appears in the image frame, which are known from scanner data. In order to solve for the unknown quantities r_{12}, r_{13}, r_{22}, r_{23}, r_{32} and r_{33}, three additional equations are needed. These can be obtained by following a similar procedure

with a shift in the z_w direction by some known increment ΔZ. This yields

$$p_3^w - p_1^w = \begin{bmatrix} 0 \\ 0 \\ \Delta Z \end{bmatrix} = R_i^w \begin{bmatrix} \Delta v_x^i \\ \Delta v_y^i \\ \Delta v_z^i \end{bmatrix} \tag{7}$$

where

$$\Delta v_x^i = p_{3x}^i - p_{1x}^i$$

$$\Delta v_y^i = p_{3y}^i - p_{1y}^i$$

$$\Delta v_z^i = p_{3z}^i - p_{1z}^i. \tag{8}$$

Equations (5) and (7) can then be solved for the second and third columns of R_{iw} as

$$r_{12} = \frac{\Delta v_x^i \Delta u_z^i - \Delta u_x^i \Delta v_z^i}{\Delta u_y^i \Delta v_z^i - \Delta u_z^i \Delta v_y^i}$$

$$r_{22} = \frac{\Delta Y \Delta v_z^i}{\Delta u_y^i \Delta v_z^i - \Delta u_z^i \Delta v_y^i}$$

$$r_{32} = \frac{-\Delta Z \Delta u_z^i}{\Delta u_y^i \Delta v_z^i - \Delta u_z^i \Delta v_y^i}$$

$$r_{13} = \frac{\Delta u_x^i \Delta v_y^i - \Delta v_x^i \Delta u_y^i}{\Delta u_y^i \Delta v_z^i - \Delta u_z^i \Delta v_y^i}$$

$$r_{23} = \frac{-\Delta Y \Delta v_y^i}{\Delta u_y^i \Delta v_z^i - \Delta u_z^i \Delta v_y^i}$$

$$r_{33} = \frac{\Delta Z \Delta u_y^i}{\Delta u_y^i \Delta v_z^i - \Delta u_z^i \Delta v_y^i} \tag{9}$$

The rotation matrix R_{iw} is then fully determined by equation (9). To mitigate the effects of measurement noise, the method outlined above can be extended to incorporate several points shifted along the y_w and z_w directions. Points measured along the y_w direction

can be fitted with a line having the form

$$l_y(t_y) = \begin{bmatrix} c^i_{y1} \\ c^i_{y2} \\ c^i_{y3} \end{bmatrix} + \begin{bmatrix} c^i_{y4} \\ c^i_{y5} \\ c^i_{y6} \end{bmatrix} t_z. \tag{10}$$

where c^i_{y1}, c^i_{y2}, c^i_{y3}, c^i_{y4}, c^i_{y5} and c^i_{y6} are constant parameters and t_y is the independent variable. Similarly, points measured along the z_w direction can be fitted with a line of the form

$$l_z(t_z) = \begin{bmatrix} c^i_{z1} \\ c^i_{z2} \\ c^i_{z3} \end{bmatrix} + \begin{bmatrix} c^i_{z4} \\ c^i_{z5} \\ c^i_{z6} \end{bmatrix} t_z. \tag{11}$$

The lines $l_y(t_y)$ and $l_z(t_z)$ represent the work frame axes y_w and z_w as viewed from the image frame. The rotation matrix R_{iw} can be solved in terms of these line parameters. Let the shifts in point positions be substituted for the line fit parameters as

$$\begin{bmatrix} c^i_{y4} \\ c^i_{y5} \\ c^i_{y6} \end{bmatrix} \rightarrow \begin{bmatrix} \Delta u^i_x \\ \Delta u^i_y \\ \Delta u^i_z \end{bmatrix} \qquad \begin{bmatrix} c^i_{z4} \\ c^i_{z5} \\ c^i_{z6} \end{bmatrix} \rightarrow \begin{bmatrix} \Delta v^i_x \\ \Delta v^i_y \\ \Delta v^i_z \end{bmatrix} \tag{12}$$

With this substitution, the only remaining unknown quantities in (9) are ΔY and ΔZ. These can be determined by taking the Euclidean norm of (5) and (7).

$$\Delta Y = \sqrt{-(\Delta u^i_x)^2 + (\Delta u^i_y)^2 + (\Delta u^i_z)^2} \tag{13}$$

$$\Delta Z = \sqrt{-(\Delta v^i_x)^2 + (\Delta v^i_x)^2 + (\Delta v^i_x)^2} \tag{14}$$

This requires that

$$(\Delta u_x^i)^2 < (\Delta u_y^i)^2 + (\Delta u_z^i)^2 \tag{15}$$

$$(\Delta v_x^i)^2 < (\Delta v_x^i)^2 + (\Delta v_x^i)^2 \tag{16}$$

and assumes that ΔY and ΔZ are positive, which is true for shifts in the positive y_w and z_w directions.

The constraint that y_i and z_i be mutually orthogonal leads to a constraint on the line parameters in (10) and (11). Substituting (10) and (11) into (2) yields the constraint

$$0 = c_{y4}^i c_{y6}^i c_{z4}^i c_{z5}^i + c_{y4}^i c_{y5}^i c_{z4}^i c_{z6}^i$$
$$- \left((c_{y5}^i)^2 + (c_{y6}^i)^2\right) c_{z5}^i c_{z6}^i - \left((c_{z5}^i)^2 + (c_{z6}^i)^2\right) c_{y5}^i c_{y6}^i \tag{17}$$

For this work, 14 scans separated by 2.5 mm were taken in the y_w direction and 20 scans separated by 4 mm were taken in the z_w direction. The lines in (10) and (11) were fitted using Matlab's fmincon. The cost function was defined as the sum of the shortest distances between the points and the lines. The distance between a data point, $\left[\Delta u_x^i, \Delta u_y^i \Delta u_z^i\right]^{\mathrm{T}}$, and a point on the line is given by

$$d(t_y) = \left\|l_y(t_y) - \Delta u^i\right\|$$
$$= \left(c_{y1}^i + c_{y4}^i t_y - \Delta u_x^i\right)^2 + \left(c_{y2}^i + c_{y5}^i t_y - \Delta u_y^i\right)^2 + \left(c_{y3}^i + c_{y6}^i t_y - \Delta u_z^i\right)^2. \tag{18}$$

The shortest distance between this point and the line can be found by

$$0 = \left. \frac{d(d(t_y))}{dt_y} \right|_{t_y = t_y^*}$$

$$= c_{y1}^i c_{y4}^i + (c_{y4}^i)^2 t_y^* - c_{y4}^i \Delta u_x^i + c_{y2}^i c_{y5}^i$$

$$+ (c_{y5}^i)^2 t_y^* - c_{y5}^i \Delta u_y^i + c_{y3}^i c_{y6}^i + (c_{y6}^i)^2 t_y^* - c_{y6}^i \Delta u_z^i$$

$$t_y^* = \frac{-c_{y1}^i c_{y4}^i + c_{y4}^i \Delta u_x^i - c_{y2}^i c_{y5}^i + c_{y5}^i \Delta u_y^i - c_{y3}^i c_{y6}^i + c_{y6}^i \Delta u_z^i}{(c_{y4}^i)^2 + (c_{y5}^i)^2 + (c_{y6}^i)^2} \tag{19}$$

Then the cost function is

$$J = \sum_{n=1}^{N_y} d(t_{y,n}^*) + \sum_{n=1}^{N_z} d(t_{z,n}^*) \tag{20}$$

where N_y is the number of points taken in the y_w direction and N_z is the number points taken in the z_w direction. Minimization was performed under the constraint given by equation (17). The fitting algorithm iterated 36 times with a final step size of 9.1e-11 and cost of 1.45 mm. The constraint was satisfied within 2.1e-19 mm^2.

Upon initial installation, the rotation transformation between the scanner and motion axes was found to be

$$R_i^w = \begin{bmatrix} 1 & 0.0092 & -0.0100 \\ 0 & 1.0000 & 0.0012 \\ 0 & -0.0012 & 1.0000 \end{bmatrix}. \tag{21}$$

The misalignment errors are indicated by the non-zero off-diagonal elements. For the 2nd and 3rd columns, which correspond to the y_i and z_i axes, errors of about 0.01 corresponded to a shift of 0.6 mm across the 60 mm measurement range in y_i and a shift of 0.96 mm over the 96 mm height measurement range.

The rotational misalignment was corrected by inserting shims near the scanner's mounting points. The scanner is mounted to the machine such that adjustments can be made about all three axes of rotation, see Figure 9. The correction will be applied as a

rotation of ϕ about the y_w axis, followed by rotations about the scanner's x and y axes.

$$Rot_{y,\phi} R_i^w Rot_{z,\psi} Rot_{x,\theta} = I$$

$$R_i^w = Rot_{y,-\phi} Rot_{x,-\theta} Rot_{z,-\psi}$$

$$= \begin{bmatrix} c\phi c\psi - s\theta s\phi s\psi & c\phi s\psi + c\psi s\theta s\phi & -c\theta s\phi \\ -c\theta s\psi & c\theta c\psi & s\theta \\ c\phi s\theta s\psi & s\phi s\psi - c\phi c\psi s\theta & c\theta c\phi \end{bmatrix} \quad (22)$$

Solving equation (22) for the angles θ, ϕ and ψ yields the following

$$\begin{cases} \theta = \text{asin}(r_{23}) \\ \phi = \text{atan2}(-r_{13}, r_{33}) \quad \text{for } \cos(\theta) > 0 \\ \psi = \text{atan2}(-r_{21}, r_{22}) \end{cases} \quad (23)$$

$$\begin{cases} \theta = \text{asin}(r_{23}) \\ \phi = \text{atan2}(r_{13}, -r_{33}) \quad \text{for } \cos(\theta) < 0 \\ \psi = \text{atan2}(r_{21}, -r_{22}) \end{cases} \quad (24)$$

According to the geometry shown in Figure 9, the appropriate thickness of shims to insert in order to correct for ϕ is $(57\text{mm})\sin(\phi)$. The shim thicknesses to add in the other locations can be found as the distances between the x_w-z_w plane and the x_i-z_i plane at the mount hole locations. After inserting shims, the identification procedure was repeated and R_{iw} was found to be

$$R_i^w = \begin{bmatrix} 1 & 0.0014 & 0.0038 \\ 0 & 1.0000 & -0.0014 \\ 0 & 0.0013 & 1.0000 \end{bmatrix} \quad (25)$$

which corresponds to a shift of 0.08 mm in y_i over the measurement range. This is acceptable considering a typical bead width is an order of magnitude larger. The shift in z_i across the height measurement range is 0.36 mm, which is significant for a measurement that spans the
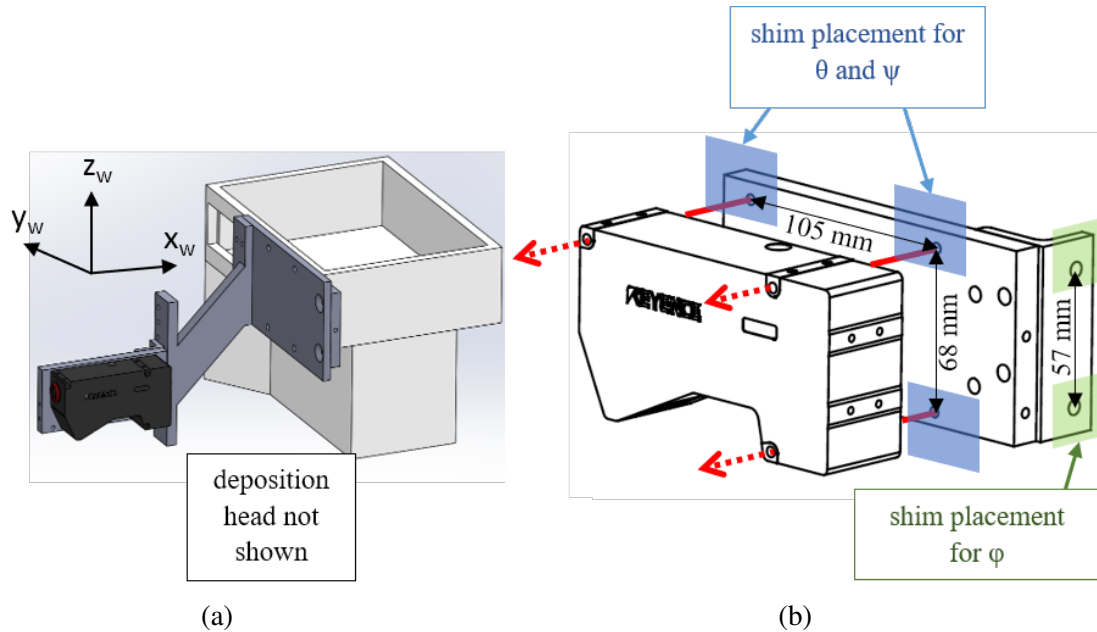
Figure 9. Mounting, (a), and shim placement, (b), for scanner alignment.

entire z_i range. However, this becomes less significant for smaller measurements obtained near the middle of the measurement range, as are obtained when scanning layer-by-layer in LMD.

4. REPEATABILITY

The laser line scanner repeatability was evaluated for three types of surfaces: 1) a matte white surface representing an ideal Lambertian surface, 2) a flat cladded surface, and 3) a surface having simple features fabricated via LMD. The matte white surface, shown in Figure 10(a), represents an ideal diffusely-reflective surface and was included as a benchmark for comparison with LMD fabricated surfaces. The cladded surface in Figure 11(a) was deposited with a hatch spacing of 0.42 mm, which corresponds to an overlap factor of 50%. The material used for both the substrate and cladding was 316L stainless steel. Lastly, a plate with LMD-fabricated features was included, see Figure 12(a).
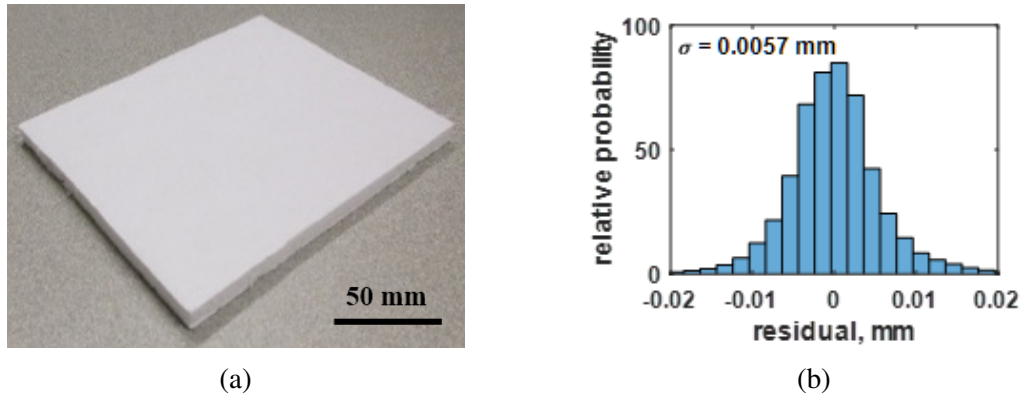
Figure 10. Matte white surface, (a), and repeatability error histogram, (b).

Each surface was scanned five times with 100 μm resolution. At each pixel location, the mean of the five trials was computed and then subtracted from the points at that location in order to center the data at zero. Then points from all locations were used to generate the repeatability error distribution. An area of 30×30 mm^2 was analyzed for the matte white and cladded surfaces, which corresponds to a total of 4.5×105 points between the five trials. For the cladded surface, repeatability tests were performed for three different scan orientations, as shown in Figure 11(a), because the texture of the cladding creates a directional dependence of the error distributions. For the feature plate data, regions containing the features were selected such that the analysis focused on measurements of the features themselves and excluded points from the surrounding substrate. Then a subset of these points was randomly selected to obtain a total of 4.5×105 points for the analysis. The histograms for the three surfaces are shown in Figures 10(b), 11(b), and 12(b) and a comparison of the results is given in Table 1.

The first column in Table 1 lists the percentage of invalid data points that were generated. As mentioned earlier, invalid data can occur when the laser reflection is not detectable due to low intensity, when multiple reflections are detected, or when there are occlusions. The white matte surface did not generate any invalid data points, as expected, since it approximates an ideal diffuse reflector. The cladded surfaces generated invalid
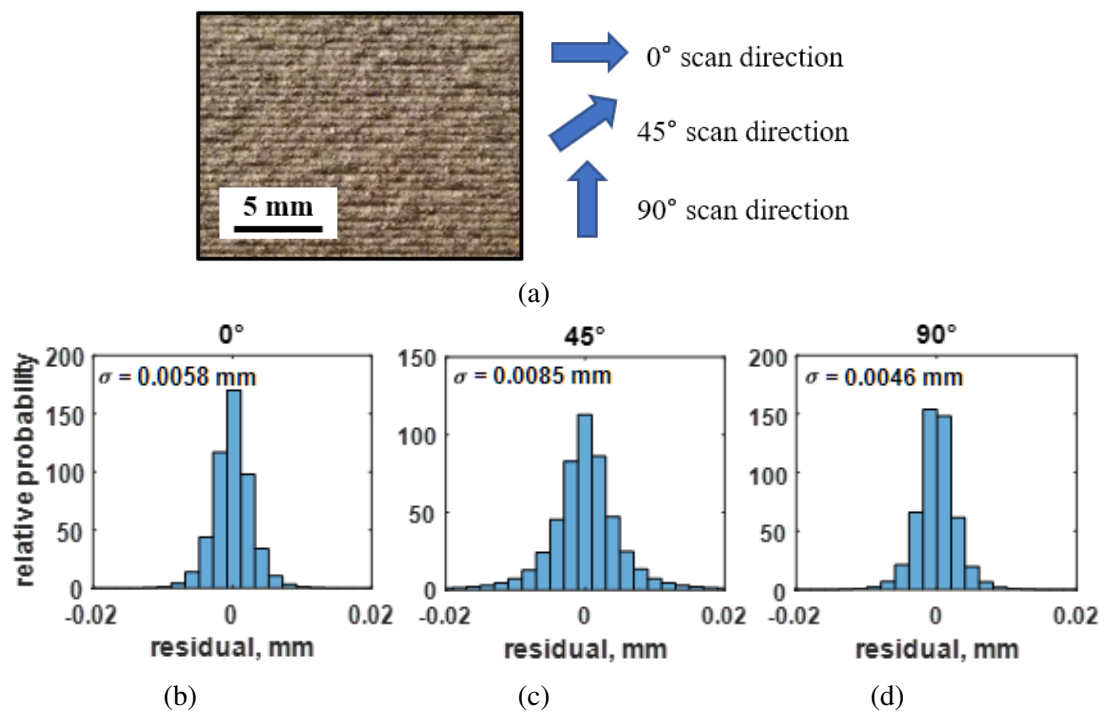
Figure 11. Cladded surface, (a), and repeatability error histograms for three scan orientations: (b) 0°, (c) 45°, (d) 90°.
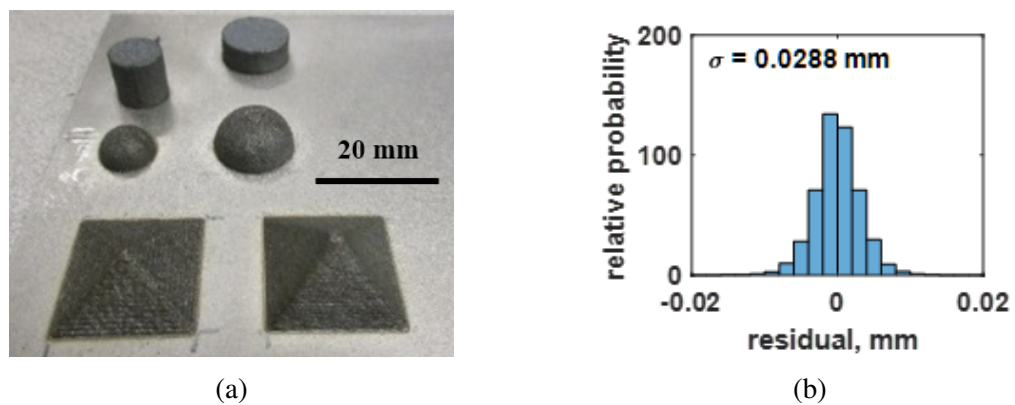
Figure 12. (a) LMD feature plate, (b) repeatability error histogram.

Table 1. Summary of repeatability results for several surface types.

surface	% in-valid points	std. dev. (mm)	min. error (mm)	max. error (mm)	range (mm)	% outliers (>0.0426 mm)
matte white	0	0.0057	-0.0424	0.0426	0.0850	0.00
clad, 0°	0.2	0.0058	-0.3548	0.4593	0.8141	0.16
clad, 45°	0.3	0.0085	-0.5811	0.4501	1.0312	0.27
clad, 90°	1.8	0.0046	-0.3699	0.3600	0.7299	0.08
feature plate	6.8	0.0519	-5.9260	8.2730	14.1990	0.55

points due to the non-uniform scattering of the laser beam, which either prevented the camera from detecting a reflection or caused the camera to detect multiple reflections. Of the three orientations, the 90° orientation creates the highest percentage of invalid points because the curvature of the beads directs the reflections away from the camera such that they are not detectable. The LMD feature plate generated the most invalid points because of both the scattering effects of cladded surfaces and the presence of surface discontinuities and occlusions, which appear in Figure 14 as blank regions surrounding the cylinders and hemispheres.

The histograms in Figures 10-12 were also plotted on a log scale in Figure 13. On a log scale, Gaussian curves appear as a straight lines such that the plots in Figure 13 feature a triangular profiles centered at zero with outliers on either side. As evident from Table 1 and the slopes of the triangular profiles in Figure 13, the matte white surface and the cladded surfaces at 0° and 90° have similar standard deviations, about 5 μm, despite having different percentages of invalid data points. Thus, although the texture of LMD surfaces creates much larger outliers than an ideal surface, the outliers are infrequent enough that their effect on the standard deviation is insignificant.

The minimum error, maximum error and error range are also included in Table 1. Despite the similar standard deviations between the matte white surface and cladded surface, the difference in error ranges is drastic – the error range for the matte white

surface is an order of magnitude less than for the other surfaces. The metric referred to as percent outliers indicates how many measurements have residuals larger than 0.0426 mm, which was the maximum residual for the white matte surface. Note that the outliers were taken as a percentage of all data points, both valid and invalid. Except for the case of the cladding scanned at 90°, the trend is that surfaces with more invalid points also generate larger standard deviations, error ranges and percentages of outliers. Although the percentage of outliers is less for the 90° orientation than for the other orientations, the combined percentage of invalid points and outliers, 1.88%, is over three times larger. Thus, scanning at 90° orientation to cladded surfaces is undesirable because it generates the largest percentage of invalid and outlier points.

In the case of the LMD feature plate, it was found that the points with the highest residuals were located at feature discontinuities where the incident beam is split between two different heights as shown in Figure 4(c) and 4(d). Figure 14 shows a top view of the LMD feature plate superimposed with points having residuals greater than 0.0426 mm.

5. ACCURACY

5.1. MEASURING LMD FEATURES

The accuracy of the laser line scanner was evaluated by inspecting the LMD feature plate shown in Figure 12(a). The deposited features were selected to include several types of basic geometries. Pyramids and hemispheres were deposited in order to investigate scanning sloped and curved surfaces, while cylinders were chosen to investigate the scanner's ability to accurately measure the height and width of LMD-fabricated parts. Using both the laser line scanner and a Coordinate Measuring Machine (CMM), the features were measured and dimensions were extracted for comparison. The CMM, a Zeiss Contura G2 (accuracy of 1.5 + [measurement length]/350 μm), was programmed to acquire points along a predetermined path with a point spacing of 1.3 mm. The resolution of the laser scanner was 100 μm in
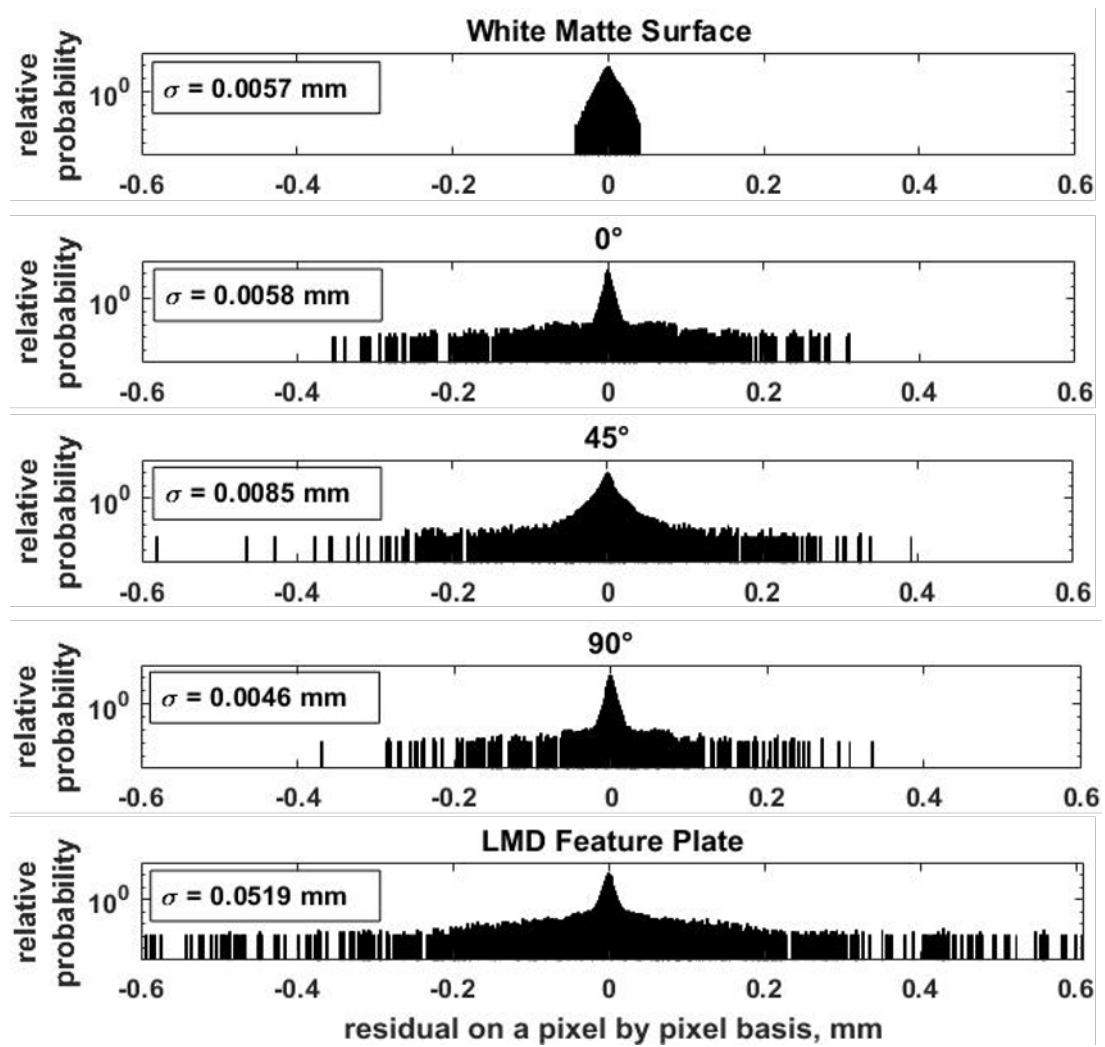
Figure 13. Histograms of repeatability errors plotted on log scale.
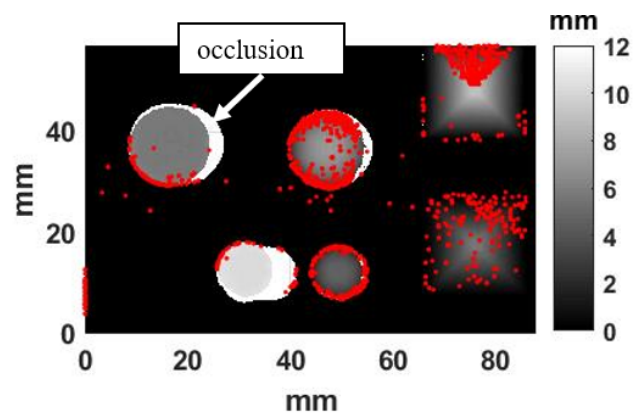
Figure 14. Top view of LMD feature plate and points with residuals >0.0426 (red dots) and occlusions (white areas).

Table 2. Feature dimensions as measured by line scanner and CMM.

feature (mm)	scanner			CMM			error	
	value	RMSE	no. pts	value	RMSE	no. pts.	abs.	%
height of short cylinder	5.794	0.044	7089	5.867	0.040	54	0.072	1.2
height of tall cylinder	10.322	0.046	2998	10.382	0.048	25	0.060	0.6
radius of short cylinder	7.869	n/a	n/a	7.932	0.033	90	0.063	0.8
radius of tall cylinder	5.407	n/a	n/a	5.442	0.043	205	0.035	0.8
curvature of small hemisphere	5.357	0.061	4608	5.370	0.046	95	0.013	0.2
curvature of large hemisphere	7.876	0.061	12025	7.872	0.049	169	-0.005	-0.1
slope of short pyramid	0.613	0.050	3684	0.608	0.057	53	-0.005	-0.8
slope of tall pyramid	1.011	0.043	4780	1.008	0.052	66	-0.003	-0.3

the x and y directions. Feature dimensions are reported in Table 2, along with the error between the CMM and scanner. The dimensions obtained from CMM measurements were taken as the reference value in calculating percent error. In order to eliminate differences due to fitting methods, identical fitting methods were used for both the scanner and CMM data, except in the case of the cylinder radii as explained below.

The fitting and feature extraction methods used to generate Table 2 are described as follows. First, a second-order polynomial was fit to the surrounding substrate regions (i.e., regions where deposition did not occur) and subtracted from the data. Since the substrate was slightly warped due to heat input, a second-order polynomial served as a better characterization than a plane fit, with correlation coefficients of 0.92 and 0.48 respectively. All feature dimensions were then taken as relative to the corrected substrate surface.

The cylinders were used to evaluate measurements of height and radii. The cylinder heights given in Table 2 were obtained by averaging points on the top of the cylinders. Cylinder radii were determined from CMM data by fitting circles to the measurements acquired around the vertical faces of the cylinders. However, the same procedure could not be applied for the scanner measurements because the scanner is unable to measure

vertical surfaces. In general, extracting lateral dimensions from top-view scans will first require identifying edges using a technique such as the Canny edge detector. Here, an edge detector and Hough transform [26]. were employed to identify the edges of the cylinder and determine the radii. In comparison with the CMM result, the scanner underestimated the radii by 63 μm (0.8%) in the case of the short cylinder and 35 μm (0.7%) for the tall cylinder. A more accurate measurement of the cylinder radii could be obtained by scanning the cylinders at an orientation such that the curved faces is visible to the scanner. Then a least-squares fitting method could be employed to fit the curved surfaces without need of an edge detector.

To obtain the hemisphere radius, a hemisphere was fitted to the measured points using the least-squares method for both the CMM and scanner data. With curvature errors of 13 μm (0.2%) for the small hemisphere and -5 μm (0.1%) for the large hemisphere, the hemisphere errors are less than the cylinder radii errors, suggesting a more accurate measurement of the cylinder radii could be obtained by scanning with a different part orientation. To determine the pyramid slopes, planes were fit to the points measured on the pyramid sides, again using a least-squares fit. The slope was taken as the Euclidean norm of the slopes in the x and y directions.

Aside from measurement noise, actual deviations of the LMD features from their nominal geometries contribute to variations in the acquire measurements. The RMSE values in Table 2 quantify the deviation of the data from the fitted surfaces, which includes both actual deviation from the nominal geometry as well as measurement noise. Between the scanner and CMM, the surface fits have similar RMSE's, even though the point density was much higher for the scanner measurements. This, combined with the fact that the RMSE are an order of magnitude greater than the 5 μm repeatability error quantified in the previous section, indicates that the RMSE values are capturing the actual deviations of the part from the nominal geometry rather than measurement noise. Except for the cylinder
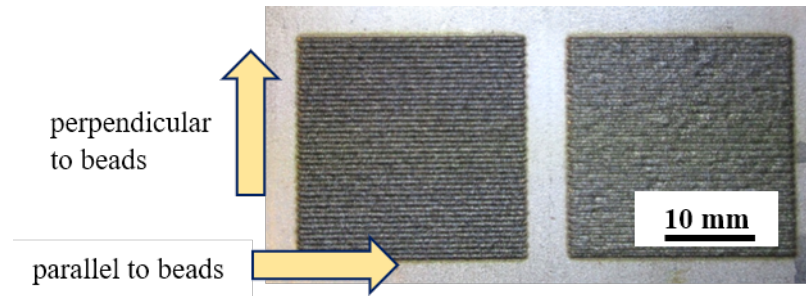
Figure 15. Cladded patches with 30% (left) and 50% (right) overlap.

heights, deviations from the fitted surfaces exceeded the error between the scanner and CMM values, indicating that the extracted dimensions are accurate with respect to the error between the nominal geometry and the features themselves.

5.2. IDENTIFYING INDIVIDUAL BEADS

When considering laser line scanning for in-process monitoring of LMD builds, the ability to distinguish individual deposited beads from each other is valuable because it allows for correlation between the measured morphology and the commanded tool path and process parameters. Here, frequency-domain techniques were leveraged to evaluate the ability to identify individual beads in cladding. Two patches of cladding were deposited with hatch spacings of 0.59 and 0.42 mm, corresponding to 30% and 50% overlap, respectively (Figure 15). The cladded patches were scanned in a direction parallel to the deposited tracks using a resolution of 100 μm in both the scan and transverse directions.

Prior to taking the 2D FFT, all invalid points were replaced with interpolated data points. The magnitude of the 2D FFT is shown in Figure 16 for the sample with 30% overlap. Due to the commanded hatch spacing of 0.59 mm, a distinct peak is expected at a frequency of 1.70 mm^{-1} in a direction perpendicular to the beads. Indeed, bright spots appear at this frequency in Figure 16. The horizontal white line indicates frequency content
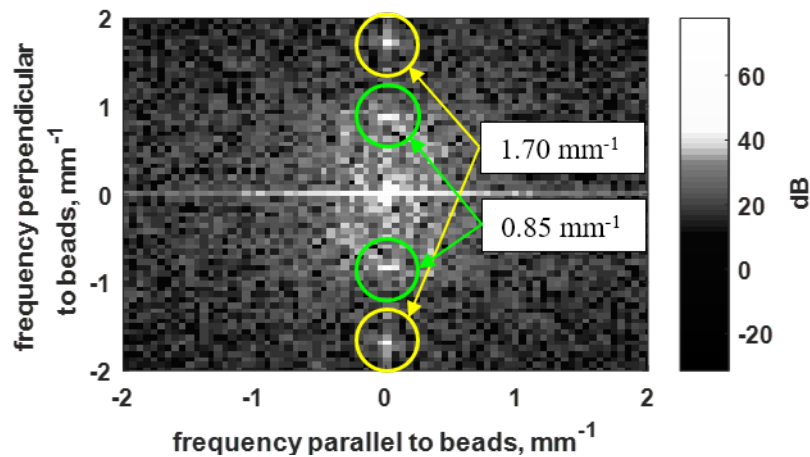
Figure 16. 2D FFT of scan of cladded surface with 30% overlap.

purely in a direction parallel to the beads. In this direction, content is observed over a range of low frequencies rather than at isolated frequencies, which indicates a lack of periodic features along the bead.

To examine frequency content purely in a direction perpendicular to the tracks, lines were extracted along the y-axis from the 2D FFT plots, and are shown below in Figure 17 for both the 30% and 50% overlap claddings. In Figure 17(a), a prominent peak appears at frequency of 1.70 mm^{-1}, which corresponds to a period of a single deposited track, and also at 0.85 mm^{-1}, which corresponds to a period of every other track. This indicates that the deposition process generates slightly different geometries with direction of travel, as each cladding track was deposited in an opposite direction of the previous track. For the cladded patch with 50% overlap, the FFT shows pronounced frequency content at 2.44 mm^{-1} due to the commanded hatch spacing of 0.42 mm, although in this case there are not prominent periodic features at the spacing of every other track. Thus, for this deposition, an overlap of 50% produced a more uniform cladding than an overlap of 30%.

In terms of the Nyquist sampling rate for this scanner, the tracks must be spaced more than 50 μm apart in order for the scanner to identify the fundamental frequency across the beads. For the bead widths deposited here, this corresponds to an overlap factor of 94%,
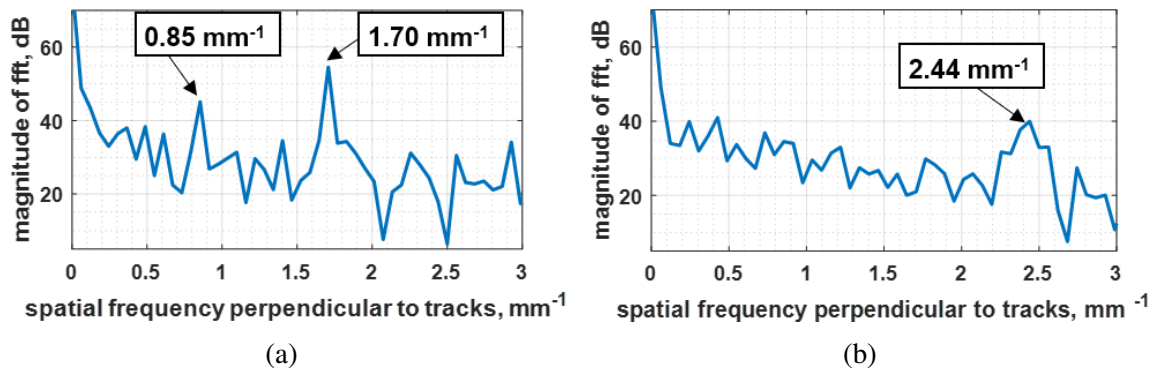
Figure 17. Magnitude for frequencies perpendicular to beads corresponding to 0 mm^{-1} in the parallel direction with (a) 30% overlap and (b) 50% overlap.

which is an unrealistic case for cladding, since even an overlap factor of 70% resulted in a cladding patch with such poor surface quality that it was not usable for this analysis. Thus, this scanner is capable of distinguishing between individual beads within the usable range of hatch spacings.

5.3. SURFACE ROUGHNESS

While the frequency domain analysis reveals the dominate frequency of the deposited cladding, surface roughness parameters indicate the energy level within a certain frequency range. To evaluate how well the laser line scanner captures the surface roughness of deposited claddings, surface roughness parameters were obtained from scan data and also from two other devices: a variable focus microscope and a contact-style profilometer. The microscope was a HiRox KH-8700, with a sampling interval of 3.88 μm, and the profilometer was a Mitutoyo SJ-201 with a sampling interval of 0.5 μm and a resolution of 0.4 μm. Prior to obtaining the measurements, loose powder was dusted off the samples with a brush. Note that with a resolution of 100 μm, the line scanner is not able to capture roughness due to individual powder particles, which have diameters in the range 36-150 μm. However the presence of the loose powder can obscure the divides between beads.

The surface roughness parameters were calculated in a direction perpendicular to the beads. Several lines were extracted from the scan data and roughness parameters were computed for each line before averaging them in order to obtain a value representative of the area. For each measured line profile, a least-squares line fit was performed and subtracted out such that the roughness parameters capture deviation from the best-fit line.

A low-pass Gaussian filter was designed with a cut-off length corresponding to 50% attenuation or about -6 dB. With hatch spacings of 0.42 and 0.59 mm, the standard cut-off length closest to the expected spatial periods and, thus, most appropriate for this case was 0.8 mm. According to ISO 11562-1996 and ASME B46-1995, the spatial-domain representation of the low-pass Gaussian filter is

$$h(x) = \frac{1}{\sqrt{\ln(2)/\pi}} \lambda_c^{-1} \exp\left(-\pi \left(\frac{x}{\sqrt{\ln(2)/\pi}} \lambda_c^{-1}\right)^2\right) \tag{26}$$

where λ_c is the cut-off length. Each line profile was low-pass filtered with the kernel in equation (26)to obtain a waviness profile. The waviness profile was then subtracted from the original profile to obtain a roughness profile. The roughness parameters R_a, R_q and R_z were evaluated over a profile length of five times the cut-off length, or 4 mm.

Four regions, each with an area 4×6.2 mm^2, were analyzed for each sample and, although the regions imaged by scanner and microscope potentially differed, the same amount of area was analyzed for both instruments. For the scanner and HiRox, the line profiles were extracted at a spacing of 0.100 mm and 62 profiles were analyzed for each region. The reported roughness parameters were averaged for the four regions. For the profilometer, the reported values represent an average of 16 lines, each 4 mm long and acquired within the area of the cladding sample. The Mean Error (ME) represents the variation in roughness parameters between the profiles, which is due to a combination of actual variation in the surface roughness throughout the sample and potentially measurement noise.

Table 3. Roughness parameters for cladding with 30% overlap. All units are μm.

	R_a	ME	R_q	ME	R_z	ME
Scanner	23	3	28	3	81	10
Microscope	28	5	33	6	96	18
Profilometer	26	8	32	9	128	38
Difference between scanner and microscope	5		5		16	
Difference between scanner and profilometer	3		4		48	

Table 4. Roughness parameters for cladding with 50% overlap. All units are μm.

	R_a	ME	R_q	ME	R_z	ME
Scanner	17	2	21	3	60	10
Microscope	15	2	18	2	51	8
Profilometer	18	2	22	3	90	11
Difference between scanner and microscope	-2		-3		-9	
Difference between scanner and profilometer	1		1		30	

For the R_a and R_q values, the errors between the measurement devices are consistently less than or equal to the mean-error among the individual profiles. This means that the variation between the profiles themselves is at least as significant as the error between the measurement devices. Despite the much lower sampling resolution of the scanner compared with the microscope, 100 μm as opposed to 3.88 μm, the scanner is able to capture the surface roughness across the tracks accurately within the actual variation of roughness throughout the sample. For the R_z values, both the variation between profiles and the discrepancy between devices is greater. This is because the R_z parameter is based on minimum and maximum values, which makes it more sensitive to the selection of slightly different evaluation regions and the presence of outliers.
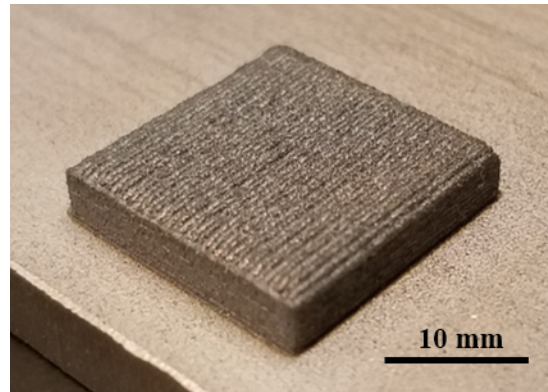
Figure 18. Photo of cube build.

Table 5. Process parameters for multi-layer build.

Parameter	Value
laser power (W)	280
laser spot size (μm)	580
powder feed rate (g/min)	11.75
print speed (mm/s)	8.5
initial nozzle stand-off (mm)	8.7
layer-to-layer nozzle increment (mm)	0.3
hatch spacing (mm)	0.46

6. LAYER-BY-LAYER SCANNING DEMONSTRATION

The usefulness of the laser scanner in collecting layer-by-layer data was demonstrated for a cube-shaped build where an interior defect was intentionally introduced (Figure 18). Ten layers were deposited where the infill orientation changed by 90° each layer. The process parameters used for this build are given in Table A.2. On the fourth layer, the laser was turned off to create a region that failed to receive material deposition. This served to simulate a defect that could arise during laser metal deposition if, for example, the powder feeder were to momentarily clog. Scans were acquired after each deposited layer, four of which are shown in Figure 19.
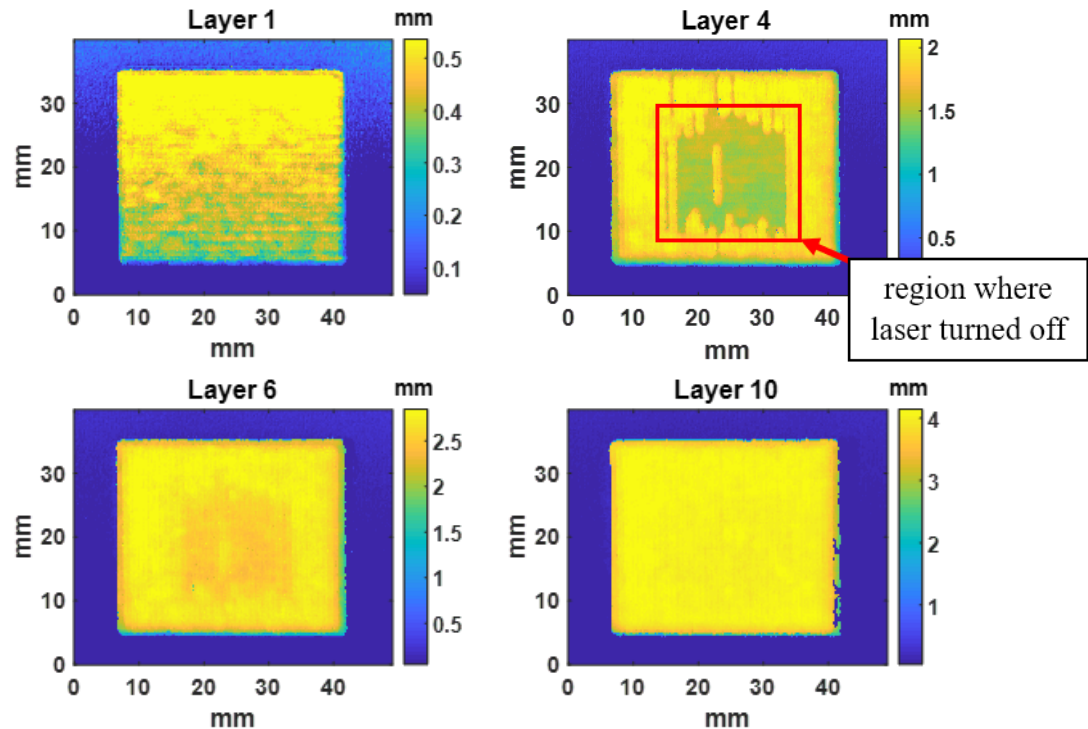
Figure 19. Scans acquired in between layers of cube build.

It can be seen in Figures 18 and 19 that the defect is not noticeable by the final layer. The build process was able to naturally recover from the defect because of the selection of the initial nozzle stand-off distance and layer-to-layer increment. The initial nozzle stand-off distance selected for this build placed the powder stream focus a distance of 0.3 mm below the build surface. As discussed in [13], the LMD process will naturally recover from height defects over the course of several layers as long as the powder stream focus remains below the build surface. The first several layers have thicknesses of approximately 0.5 mm. As more layers are deposited, the layer thickness approaches 0.3 mm, which is the nozzle increment between layers. The convergence of layer thickness to the commanded layer-to-layer increment is expected behavior for builds that occur in the self-stabilizing region of the powder catchment profile. The lack of growth in the defective region is clearly evident on the fourth layer. Figure 20 shows average layer thicknesses in the non-defective and defective regions. After the fourth layer, the defective region experiences
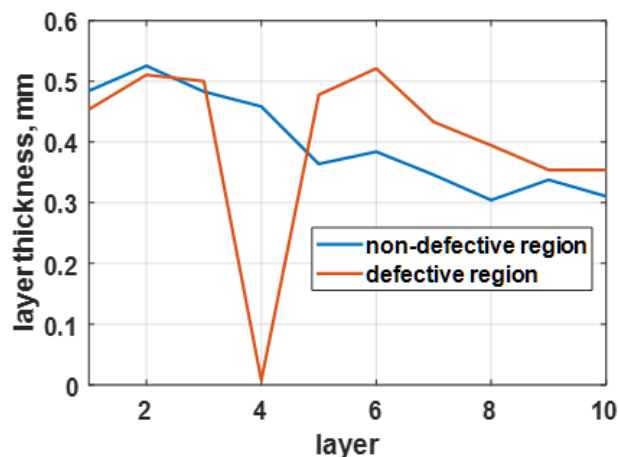
Figure 20. Layer thicknesses for cube build.

thicker deposits than the non-defective region, again because the underbuilt regions receive more powder when operating in the self-stabilizing region of the powder catchment profile. By the tenth layer, it appears that the deposition thickness in the defective region approaches that of the non-defective region, recovering the nominal layer thickness. While the part ultimately achieves the desired geometry, several layers of larger-than-expected thickness may necessitate additional testing to assure qualification. Here it is demonstrated that the layer-by-layer scanning strategy provides information regarding interior part defects that would not be evident by visual inspection of the final part exterior.

7. SUMMARY AND CONCLUSIONS

Various aspects of using a laser line scanner in an LMD application were explored. A method of identifying and correcting misalignment between the scanner and motion axis was presented. Repeatability and accuracy were evaluated for LMD surfaces. The repeatability error distribution for an LMD cladded surface was found to have outliers due to specular reflections. Although the outliers had large residuals, up to 0.6 mm for the cladded surface and 8.3 mm for the LMD feature plate, they were infrequent enough that they did not notably affect the noise level as captured by the standard deviations.

The orientation of the cladded tracks with respect to the laser line affected the amount of invalid data produced and the presence of outliers. Although scanning perpendicular to the deposited beads produced more invalid data points than scanning parallel, 1.8% as opposed to 0.2% invalid points, the standard deviations of the valid data were comparable, 5.8 μm and 4.6 μm. When measuring LMD specimens such as cylinders, hemispheres, and pyramids, the points with the largest repeatability error were found to be located at the vertical edges of the features. To assess the accuracy of part dimensions obtained from scanner data, the LMD features were measured with both the scanner and a CMM, and comparison was made between the resulting part dimensions. The dimensions from the laser line scanner differed from CMM data by no more than 1.2%. Frequency-domain techniques were leveraged to determine that the scanner was able to distinguish between individual tracks. The ability of the scanner to detect surface roughness was also evaluated. Roughness parameters were computed from scanner data of a cladded surface and compared with roughness parameters from data obtained with a HiRox microscope and a contact-style profilometer. The variation of the roughness parameters within the cladding sample was greater than the error between the scanner and HiRox, meaning that the line scanner can measure surface roughness accurately within the roughness variation of the surface itself. Lastly, the application of laser line scanning to in-process sensing for LMD builds was demonstrated. A history of layer geometry proves useful in identifying internal defects that may not be evident in the final product, yet may compromise the material properties of the part.

ACKNOWLEDGEMENTS

REFERENCES

[1] Huang, Y., Leu, M. C., Mazumder, J., and Donmez, A., 'Additive manufacturing: current state, future potential, gaps and needs, and recommendations,' Journal of Manufacturing Science and Engineering, 2015, **137**(1).

[2] Jurrens, K., 'Energetics incorporated, measurement science roadmap for metal-based additive manufacturing,' Addit. Manuf, 2013, **86**.

[3] Bourell, D., Leu, M., and Rosen, D., 'Identifying the future of freeform processing,' Roadmap for Additive Manufacturing. Austin: The University of Texas, 2009.

[4] Everton, S. K., Hirsch, M., Stravroulakis, P., Leach, R. K., and Clare, A. T., 'Review of in-situ process monitoring and in-situ metrology for metal additive manufacturing,' Materials & Design, 2016, **95**, pp. 431–445.

[5] Ding, Y., Warton, J., and Kovacevic, R., 'Development of sensing and control system for robotized laser-based direct metal addition system,' Additive Manufacturing, 2016, **10**, pp. 24–35.

[6] Hu, D. and Kovacevic, R., 'Sensing, modeling and control for laser-based additive manufacturing,' International Journal of Machine Tools and Manufacture, 2003, **43**(1), pp. 51–60.

[7] Song, L., Bagavath-Singh, V., Dutta, B., and Mazumder, J., 'Control of melt pool temperature and deposition height during direct metal deposition process,' The International Journal of Advanced Manufacturing Technology, 2012, **58**(1), pp. 247–256.

[8] Iravani-Tabrizipour, M. and Toyserkani, E., 'An image-based feature tracking algorithm for real-time measurement of clad height,' Machine Vision and Applications, 2007, **18**(6), pp. 343–354.

[9] Barua, S., Sparks, T., and Liou, F., 'Development of low-cost imaging system for laser metal deposition processes,' Rapid Prototyping Journal, 2011.

[10] Kummailil, J., Sammarco, C., Skinner, D., Brown, C. A., and Rong, K., 'Effect of select lens™ processing parameters on the deposition of ti-6al-4v,' Journal of manufacturing processes, 2005, **7**(1), pp. 42–50.

[11] Davis, T. A. and Shin, Y. C., 'Vision-based clad height measurement,' Machine Vision and Applications, 2011, **22**(1), pp. 129–136.

[12] Tang, L. and Landers, R. G., 'Layer-to-layer height control for laser metal deposition process,' Journal of Manufacturing Science and Engineering, 2011, **133**(2).

[13] Sammons, P. M., Gegel, M. L., Bristow, D. A., and Landers, R. G., 'Repetitive process control of additive manufacturing with application to laser metal deposition,' IEEE Transactions on Control Systems Technology, 2018, **27**(2), pp. 566–575.

[14] Gegel, M. L., Bristow, D. A., and Landers, R. G., 'A quadratic-optimal repetitive process controller for laser metal deposition,' in '2018 Annual American Control Conference (ACC),' IEEE, 2018 pp. 4446–4451.

[15] Doumanidis, C. and Kwak, Y.-M., 'Geometry modeling and control by infrared and laser sensing in thermal manufacturing with material deposition,' J. Manuf. Sci. Eng., 2001, **123**(1), pp. 45–52.

[16] Heralić, A., Christiansson, A.-K., and Lennartson, B., 'Height control of laser metal-wire deposition based on iterative learning control and 3d scanning,' Optics and lasers in engineering, 2012, **50**(9), pp. 1230–1241.

[17] Borish, M., Post, B. K., Roschli, A., Chesser, P. C., Love, L. J., and Gaul, K. T., 'Defect identification and mitigation via visual inspection in large-scale additive manufacturing,' JOM, 2019, **71**(3), pp. 893–899.

[18] Stavroulakis, P. and Leach, R. K., 'Invited review article: review of post-process optical form metrology for industrial-grade metal additive manufactured parts,' Review of Scientific instruments, 2016, **87**(4), p. 041101.

[19] Wang, Y. and Feng, H.-Y., 'Effects of scanning orientation on outlier formation in 3d laser scanning of reflective surfaces,' Optics and Lasers in Engineering, 2016, **81**, pp. 35–45.

[20] Vukašinović, N., Možina, J., and Duhovnik, J., 'Correlation between incident angle, measurement distance, object colour and the number of acquired points at cnc laser scanning,' Strojniški vestnik-Journal of Mechanical Engineering, 2012, **58**(1), pp. 23–28.

[21] Isheil, A., Gonnet, J.-P., Joannic, D., and Fontaine, J.-F., 'Systematic error correction of a 3d laser scanning measurement device,' Optics and Lasers in Engineering, 2011, **49**(1), pp. 16–24.

[22] Reiner, J. and Stankiewicz, M., 'Verification of the predictive segmentation algorithm for the laser triangulation method,' Metrology and Measurement Systems, 2011, **18**(4), pp. 667–678.

[23] Curless, B. and Levoy, M., 'Better optical triangulation through spacetime analysis,' in 'Proceedings of IEEE International Conference on Computer Vision,' IEEE, 1995 pp. 987–994.

[24] Feng, H.-Y., Liu, Y., and Xi, F., 'Analysis of digitizing errors of a laser scanning system,' Precision Engineering, 2001, **25**(3), pp. 185–191.

[25] Baribeau, R. and Rioux, M., 'Influence of speckle on laser range finders,' Applied optics, 1991, **30**(20), pp. 2873–2878.

[26] Nixon, M. and Aguado, A., *Feature extraction and image processing for computer vision*, Academic press, 2019.

II. QUADRATIC OPTIMAL CONTROL FOR LASER METAL DEPOSITION

Michelle L. Gegel
Department of Mechanical & Aerospace Engineering
Missouri University of Science and Technology
Rolla, Missouri 65409–0050

Douglas A. Bristow
Department of Mechanical & Aerospace Engineering
Missouri University of Science and Technology
Rolla, Missouri 65409–0050
Tel: 573–341–6559
Email: dbristow@mst.edu

Robert G. Landers
Department of Aerospace & Mechanical Engineering
University of Notre Dame
Email: rlanders@nd.edu

ABSTRACT

In Laser Metal Deposition (LMD), metal powder is blown from a nozzle into a laser-formed melt pool and parts are fabricated layer-by-layer. Here, LMD is modeled as a repetitive process where layers are added iteratively and each layer is affected by previous layers. In order to control part height during a build, measurements are taken in between layers and corrections are applied during the next layer by adjusting the nozzle speed along the deposition path. The quadratic optimal control design, a widely used approach, is here extended to the class of repetitive processes and specifically to LMD. The framework was then extended to the case of a closed-contour tool path, that is, a path whose beginning and end points coincide. The controller demonstrated the ability to significantly improve geometric accuracy in LMD parts.

Keywords: metal additive, laser metal deposition, quadratic optimal control, repetitive process control

1. INTRODUCTION

Laser Metal Deposition (LMD) is a manufacturing process where material is deposited by blowing metal powder into a laser-formed melt pool and parts are fabricated layer-by-layer. Unlike powder-bed processes, laser metal deposition can deposit on existing parts which makes it useful for repairing high-value parts such as die tooling, or turbine blades [1, 2, 3]. In addition, LMD is capable of producing functionally-graded parts, for which the material composition varies throughout the part geometry, by controlling the mixture ratio of powder fed through the nozzle [4, 5, 6].

However, achieving geometrically accurate builds in LMD is challenging. This is because deposition quality depends on process inputs that are subject to non-deterministic fluctuations as well as environmental conditions. In [3], a factorial experiment was conducted and it was found that the bead height is most influenced by the powder feed, followed by nozzle speed and laser power. Another very significant process parameter is stand off distance [7, 8]. Environmental conditions can vary throughout the course of the build, in particular due to heat accumulation [9]. Thus, maintaining consistent bead morphology requires adjustments in the process inputs throughout the build. Deposition is also influenced by the geometry of previous layers such that errors, once initiated, often propagate through the part and sometimes amplify [7]. For these reasons, closed-loop feedback control is needed to maintain quality deposition in LMD and has been recognized as a key aspect in advancing the technology [10, 11].

Several researchers have controlled the melt pool temperature by adjusting the laser power. Saheli et al. demonstrated closed-loop temperature control for single-layer cladding. Although the controller successfully tracked the temperature set-point, the clad thickness was seen to vary with the addition of tracks side-by-side [12]. Tang and Landers sought to control temperature via laser power for thin wall builds [13]. Their approach used an empirically-identified model of the relationship between laser power and melt pool temperature and a model-inverse based controller. Both of these papers concluded

that maintaining a constant temperature was not enough guarantee consistent deposition morphology. In [14], temperature control was paired with a path-dependent temperature reference for thin wall builds. Decreasing the temperature near the edges of the thin wall was found to reduce excess build-up and shrinkage error at the edges as well as improve microstructure.

Other approaches use the melt pool size, as measured with a CCD camera, as the process output to control. In [15], laser power is adjusted to achieve the desired bead height. The closed-loop build appears less defective than the open-loop case. Ding et. al also controlled melt pool size by adjusting laser power, but included an independent feedback loop around the powder feed [16]. Powder feed, although not commonly used as a control input for LMD, was used to achieve the desired height in [17]. Particle Swarm Optimization updated the model parameters layer based on height and temperature measurements of the previous layer. In [18], nozzle speed, rather than laser power, was used to achieve the desired bead height. Here, PID was combined with feedforward control, which improved tracking of clad references with varying height.

Measurements of the processing zone are challenging due to the high temperatures and radiation levels. Furthermore, any adjustments made to the process inputs in response to measurements may improve future deposition quality but cannot correct defects that have already occurred. For these reasons, an effective control strategy is to apply corrections for a measured defect on the following layer. This allows the corrections to be applied at the precise location of the defects. Heralic, et. al. employed this strategy to control part height in a wire-fed metal additive process [19]. More generally, the idea of feeding corrections forward to the next iteration of a process is known as Iterative Learning Control (ILC). In ILC, the output of each iteration is assumed to be independent of previous iterations' outputs. This is not the case for LMD, since the effects of previous layers influence the

deposition behavior on the current layer. Thus LMD is best considered as a repetitive process, in which outputs from previous iterations directly influence outputs for the current iteration.

The work here builds off of the repetitive process model for LMD developed by Sammons [20]. The model characterizes the relationship between the commanded nozzle speed along the toolpath and the resulting deposition height. We use this model to propose a quadratic optimal controller for a repetitive process. To implement the proposed controller, the part height is measured after each layer with an optical scanner and the nozzle speed trajectory is adjusted for the next layer. The quadratic optimal formulation was first presented for a repetitive process in [21] with preliminary experimental results. Here the formulation has been extended to the case of a closed tool path, that is, a tool path with coincident starting and ending points.

Section 2 describes the repetitive process model, which is used later in the control design. Section 3 develops the quadratic optimal controller for a generic repetitive. In Section 4, the model and controller are extended to the case of a closed-contour tool path in LMD. Experimental results are presented in Section 5.

2. REPETITIVE PROCESS MODEL FOR LMD

An LMD process model was introduced in [22] and [20]. For completeness, the model is briefly presented here. The model describes the morphology of a deposited track in two dimensions: 1. along the build path, represented by the independent variable x, and 2. at each layer, represented by the discrete variable j. The model relates commanded inputs, such as the z-increment between layers and the nozzle velocity, to the resulting bead height, while also incorporating the effect of previous layers. The resulting model was nonlinear and then was linearized about a nominal operating point.
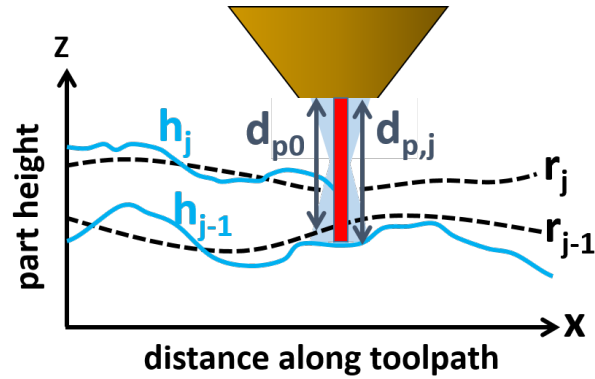
Figure 1. Diagram of variable designations.

The part height, $h(x, j)$, is modeled as

$$h(x, j) = b_0^{-1}\zeta f_\mu(d_p(x, j))\lambda(x, j) * f_s(x)$$
$$+ h(x, j - 1) * f_r(x) \qquad (1)$$

or more compactly,

$$h_j = b_0^{-1}\zeta f_\mu(d_{p,j})\lambda_j * f_s + h_{j-1} * f_r \qquad (2)$$

where the argument x has been omitted and the argument j is indicated by a subscript, h_j is the part height (mm) after depositing the jth layer, λ_j is the commanded spatial mass flow (g/mm) that produced h_j, $d_{p,j}$ is the nozzle standoff distance (mm) prior to depositing the jth layer, b_0 is the estimated bead width (mm), ζ is the material specific volume (m^3/g), $f_\mu()$ is the powder catchment function, $f_s()$ is the shaping function, and $f_r()$ is the remelt function. The physical meanings of these variables are given in Fig. 1. The shaping and

remelt functions in (2), respectively, are given by

$$f_s(x) = \begin{cases} \frac{2}{l^2}(x - \delta) & \delta \leq x \leq \delta + l \\ 0 & \text{otherwise} \end{cases} \tag{3}$$

$$f_r(x) = \begin{cases} \frac{1}{l_r} - |\frac{x}{l_r^2}| & -l_r \leq x \leq l_r \\ 0 & \text{otherwise} \end{cases} \tag{4}$$

where l, l_r, and δ are model parameters found empirically from system identification techniques. The interested reader is referred to [22] and [20] for a detailed description of these parameters and how they are determined experimentally. The function f_μ represents powder catchment efficiency and is a nonlinear function of stand-off distance, $d_p(x, j)$, given by

$$f_\mu(d_{p,j}) = \frac{\alpha_{max}}{100} \exp\left[-\left[\frac{d_{p,j} - d_{max}}{\alpha_{width}}\right]^2\right] \tag{5}$$

where the parameters α_{max}, d_{max}, and α_{width} are determined empirically.

We assume that the nozzle is always a fixed distance d_{p0} above the previous layer's reference height, denoted r_{j-1}. Then the distance between the nozzle and the surface on which it is depositing is

$$d_p = d_{p0} + r_{j-1} - h_{j-1}. \tag{6}$$

Using (6), the nonlinear powder catchment function can be linearized with respect to h_{j-1} and r_{j-1}. We choose the same stationary point for the previous layer's height and reference, $h_{j-1,e} = r_{j-1,e}$, and linearize (2) using Taylor's series approximation. This yields

$$h_j \approx (\kappa_1 \lambda_j - \kappa_2(h_{j-1} - r_{j-1})) * f_s + h_{j-1} * f_r \tag{7}$$

where

$$\kappa_1 = b_0^{-1} \zeta f_\mu(d_{p0}) \tag{8}$$

$$\kappa_2 = -b_0^{-1} \zeta \lambda_{j,e} \frac{2}{\alpha_{width}^2} (d_{p0} - d_{max}) f_\mu(d_{p0}). \tag{9}$$

Let the height error be defined as $e_j(x) = r_j(x) - h_j(x)$ and assume that the desired layer thickness is constant for each layer: $(r_{j+1} - r_j) = (r_j - r_{j-1}), \forall j \geq 1$. Then the error dynamics of the repetitive process are given by

$$e_j(x) = a(x) * e_{j-1}(x) + b(x) * \lambda_j(x) + d(x) \tag{10}$$

where $d(x)$ is an exogenous, iteration-invariant disturbance and

$$a(x) = f_r(x) - \kappa_2 f_s(x) \tag{11}$$

$$b(x) = -\kappa_1 f_s(x) \tag{12}$$

We will work with the lifted-representation of (10):

$$\mathbf{e_j} = \mathbf{A e_{j-1}} + \mathbf{B} \lambda_{\mathbf{j}} + \mathbf{d}. \tag{13}$$

The vectors $\mathbf{e_j}$, $\mathbf{e_{j-1}}$, $\lambda_{\mathbf{j}}$, and $\mathbf{d}$ are the spatial signals which have been sampled discretely over a finite range, for example

$$\mathbf{e_j} = [e_j(0), e_j(\Delta x), ...e_j(M\Delta x)]^{\mathrm{T}}. \tag{14}$$

The matrix $\mathbf{A}$ is constructed by sampling $a(x)$ and arranging the sampled values as a convolution matrix.

$$\mathbf{A} =$$

$$
\begin{bmatrix}
a(0) & a(-\Delta x) & \cdots & a(-N_L\Delta x) & 0 & \cdots & & 0 \\
a(\Delta x) & a(0) & & \cdots & & & & \vdots \\
\vdots & & \ddots & & & & & 0 \\
a(N_R\Delta x) & & & \ddots & & & a(-N_L\Delta x) \\
0 & & & & \ddots & & & \vdots \\
\vdots & & & & & a(0) & a(-\Delta x) \\
0 & \cdots & 0 & a(N_R\Delta x) & \cdots & a(\Delta x) & a(0)
\end{bmatrix}
\tag{15}
$$

where Δx is the spatial sampling resolution and N_L and N_R define the finite support of $a(x)$. The matrix $\mathbf{B}$ is similarly constructed.

3. QUADRATIC OPTIMAL CONTROL FORMULATION

We define the cost function in the traditional way as

$$J = \mathbf{e_j}^\mathrm{T}\mathbf{Q}\mathbf{e_j} + (\lambda_\mathbf{j} - \lambda_{\mathbf{j-1}})^\mathrm{T}\mathbf{R_j}(\lambda_\mathbf{j} - \lambda_{\mathbf{j-1}}) + \lambda_\mathbf{j}^\mathrm{T}\mathbf{S_j}\lambda_\mathbf{j} \tag{16}$$

where $\mathbf{Q}$, $\mathbf{R}$, and $\mathbf{S}$ are positive definite matrices selected by the designer. In implementation, the error for the jth layer, $\mathbf{e_j}$, is not known until after the input $\lambda_\mathbf{j}$ is applied. Thus to solve for the optimal $\lambda_\mathbf{j}$ we use the model equation (13) to express the current error in terms of previous-layer quantities.

$$
\begin{aligned}
J =& (\mathbf{A}\mathbf{e_{j-1}} + \mathbf{B}\lambda_\mathbf{j} + \mathbf{d})^\mathrm{T}\mathbf{Q}(\mathbf{A}\mathbf{e_{j-1}} + \mathbf{B}\lambda_\mathbf{j} + \mathbf{d}) \ldots \\
& + (\lambda_\mathbf{j} - \lambda_{\mathbf{j-1}})^\mathrm{T}\mathbf{R_j}(\lambda_\mathbf{j} - \lambda_{\mathbf{j-1}}) + \lambda_\mathbf{j}^\mathrm{T}\mathbf{S_j}\lambda_\mathbf{j}
\end{aligned}
\tag{17}
$$

Solving for the optimal j^{th} layer control, $\lambda_\mathbf{j}^{opt}$, we have

$$0 = \left.\frac{\partial J}{\partial \lambda_j}\right|_{\lambda_j^{opt}} = 2\mathbf{B}^\mathrm{T}\mathbf{QB}\lambda_\mathbf{j}^{opt} + 2\mathbf{B}^\mathrm{T}\mathbf{Q}(\mathbf{Ae_{j-1}} + \mathbf{d})\ldots$$

$$+ 2\mathbf{R}\lambda_\mathbf{j}^{opt} - 2\mathbf{R}\lambda_\mathbf{j-1} + 2\mathbf{S}\lambda_\mathbf{j}^{opt} \tag{18}$$

Again, using the model equation and leveraging the fact that $\mathbf{d}$ is iteration-invariant, we substitute $\mathbf{d} = \mathbf{e_{j-1}} - \mathbf{Ae_{j-2}} - \mathbf{B}\lambda_\mathbf{j-1}$ to eliminate the unknown disturbance and rearrange to obtain

$$\lambda_\mathbf{j}^{opt} = \mathbf{L_e e_{j-1}} + \mathbf{L_\lambda}\lambda_\mathbf{j-1} + \mathbf{L_{de}}(\mathbf{e_{j-1}} - \mathbf{e_{j-2}}) \tag{19}$$

where

$$\mathbf{L_e} = (\mathbf{B}^\mathrm{T}\mathbf{QB} + \mathbf{R} + \mathbf{S})^{-1}(-\mathbf{B}^\mathrm{T}\mathbf{Q})$$

$$\mathbf{L_\lambda} = (\mathbf{B}^\mathrm{T}\mathbf{QB} + \mathbf{R} + \mathbf{S})^{-1}(\mathbf{B}^\mathrm{T}\mathbf{QB} + \mathbf{R})$$

$$\mathbf{L_{de}} = (\mathbf{B}^\mathrm{T}\mathbf{QB} + \mathbf{R} + \mathbf{S})^{-1}(-\mathbf{B}^\mathrm{T}\mathbf{QA}). \tag{20}$$

This solution contains terms that play the roles of a PID controller, but in layer-domain rather than in temporal domain. The form of the quadratic optimal problem formulated here is analogous to the popular Norm-Optimal Iterative Learning Control (NO-ILC) problem, which applies to the special case for $\mathbf{A} = 0$ above. Compared to the NO-ILC solution, the iteration-domain integrator pole at $-\mathbf{L_\lambda}$ and negative feedback gain, $\mathbf{L_e}$, are the same. However, an additional iteration-domain derivative term, $-\mathbf{L_{de}}$ appears in the solution to address the A dynamics of the repetitive process problem.

4. MATRIX STRUCTURE FOR CLOSED PATHS

The lifted form of the model in (15) has a single spatial dimension and allows points that are near *along the toolpath* to influence each other. I.e. material deposited at a given location can spread to locations ahead of or behind the current position along the toolpath. However, if the toolpath has curvature, two locations can be far apart with respect to the toolpath and yet near to each other in the x-y plane. For this reason, others have employed 2D spatial models to describe manufacturing processes [23, 24, 25]. To extend this work to the case of a path-dependent model, we will here consider a toolpath that interacts with itself at one point: the beginning and end of a closed-contour.

In the literature, over-build at the toolpath's beginning and end is often observed because the laser remains on during the nozzle acceleration/deceleration. In this work, however, the motion system appends lead-in and lead-out motions to the deposition pass, during which the laser is off. Although deposition does not occur during the acceleration or deceleration phases of motion, overbuild at the ends is still observed. Thus, the process itself must have start-up dynamics that lead to build-up at the toolpath ends. In [26], Li developed a model that did not include the affects of motion acceleration and yet the model predicted slight overbuild at the ends, particularly when there was less cooling time in between layers.

Overbuild at the beginning and end of a deposition can be especially problematic for a toolpath that is a closed-contour, that is a continuous motion where the beginning and end points coincide. Typically toolpaths for AM parts include closed-contours in addition to raster infill patterns. When the deposition path is a closed contour, accumulation of height error at the seam can lead to an unusable part. To avoid compounding defects at the start/stop of closed contours, some have changed where the path starts each layer [2, 27]. Here we will extend the model - and the derived controller - to the case of a toolpath that has coincident beginning and end points.

For a toolpath with coincident beginning and end points, the signals $h(x)$, $r(x)$, and $\lambda(x)$ are periodic with a period of the toolpath length. Then the height output can be taken as the periodic convolution

$$h_j(x) = \kappa_1 f_s(x) \circledast \lambda_j(x) + f_r(x) \circledast h_{j-1}(x) \tag{21}$$

This operation involves wrapping the elements from the end of the toolpath to the beginning and vice-versa. In lifted form the convolution matrices now include off-diagonal elements, making it a circulant matrix.

$$
\mathbf{A} =
\begin{bmatrix}
a(0) & \cdots & a(-N_L\Delta x) & 0 & \cdots & a(N_R\Delta x) & \cdots & a(\Delta x) \\
\vdots & \ddots & & & & & & \vdots \\
\vdots & & & & & & & a(N_R\Delta x) \\
a(N_R\Delta x) & & & & & & & 0 \\
0 & & & & & & & \vdots \\
\vdots & & & & & & & a(-N_L\Delta x) \\
a(-N_L\Delta x) & & & & & & & a((-N_L+1)\Delta x) \\
\vdots & & & & & \ddots & & \vdots \\
a(-\Delta x) & \cdots & a(-N_L\Delta x) & 0 & \cdots & a(N_R\Delta x) & \cdots & a(0)
\end{bmatrix}
\tag{22}
$$

5. EXPERIMENTAL RESULTS

Experiments were performed on a 5-axis LMD machine at Missouri S&T. This system includes an Optomec LENS Print Engine (LPE), an Optomec powder feeder, a 1kW ytterbium laser (IPG YLR-1000-MM-WC-Y14), which are all centrally controlled by a National Instruments PXI (PXI-8186) running LabVIEW Real-Time 17.0.0. The motion-control portion of the LabVIEW code executes a rate of 5,000 Hz. Feedback height

measurements are obtained between layers using a laser line scanner (Keyence LJ-V7200), which has a resolution of 0.001 mm in the vertical direction and 0.1 mm along the laser line. The repeatability on cladded surfaces has been found to be 0.006 mm. The measurements are triggered from the x-axis encoder, ensuring precise spacing between measurement points and correlation between the scan data and machine toolpath. The encoder resolution is 0.25 μm and the scanner is set to trigger every 0.1 mm. Measurement noise is filtered using a low-pass Gaussian filter with a cut-off length of 1.2 mm, approximately equal to the melt pool length. The material used is 316L stainless steel, with a diameter range 53 - 150 μm. The model and process parameters for the experiments are given in Tables A.1 and A.2.

The control input given by (19) is converted to a velocity trajectory according to

$$v_j(x) = \frac{\lambda_0 v_0}{\lambda_j(x)} \tag{23}$$

where v_0 is the nominal velocity (mm/s) and λ_0 is the nominal spatial mass flow rate (g/mm). Since the control law in (19) can generate negative or zero values for λ, (23) could result in negative or infinite velocity values respectively. These are infeasible to implement since the process cannot remove material by moving backwards along the toolpath; neither can the machine cannot move at an infinite velocity. Thus, a maximum velocity threshold is applied to (23) based on what is achievable for the machine. Whenever the maximum velocity threshold is active, the laser power is reduced by half to decrease the bead height at those locations. As mentioned earlier, lead-in and lead-out motions are appended to the controller-generated velocity such that the machine does not deposit during the acceleration/deceleration phases of motion at the beginning and end of deposition passes. Since the motion control for the machine is position-based, the velocity profile is converted to a position profile in time, which is fed point-by-point as reference to the motion controller.

Table 1. Model Parameters

Parameter	Symbol	Value
melt pool length, mm	l	1.01
melt pool shift, mm	δ	-0.91
remelt length, mm	l_r	0.52
melt pool width, mm	b_0	0.8
max powder catchment	α_{max}	0.056
catchment width, mm	α_{width}	3.0
powder focal distance, mm	d_{max}	9.4
nominal speed, mm/s	v_0	8.5
nominal mass addition, g/mm	λ_0	0.0275

Table 2. Process Parameters

Parameter	Value
laser power, W	300
powder feed rate, g/s	0.23
initial stand-off distance, mm	8.5
z-increment, mm	0.25

Two part geometries were built: a thin wall and a cylinder. Each part was built with and without feedback control. For the builds without control, a constant nozzle speed and laser powder was commanded for the entire length of the tool path. The nozzle speed for the open-loop builds was determined from the desired layer thickness and the DC gain of the model-inverse.

The control matrices, **Q**, **R** and **S** were selected to be unity matrices each multiplied by a different scaling factor. Suitable choices for these scaling factors were found empirically as 1, 0.25, and 0.5 respectively.

5.1. THIN WALL PART

The thin walls were designed to be 40 mm long and 5 mm tall with a total of 20 layers. The open-loop wall shows several geometric inaccuracies (Figure 2). First, ripples that initiate on the very first layer are seen to amplify in every subsequent layer. Second,
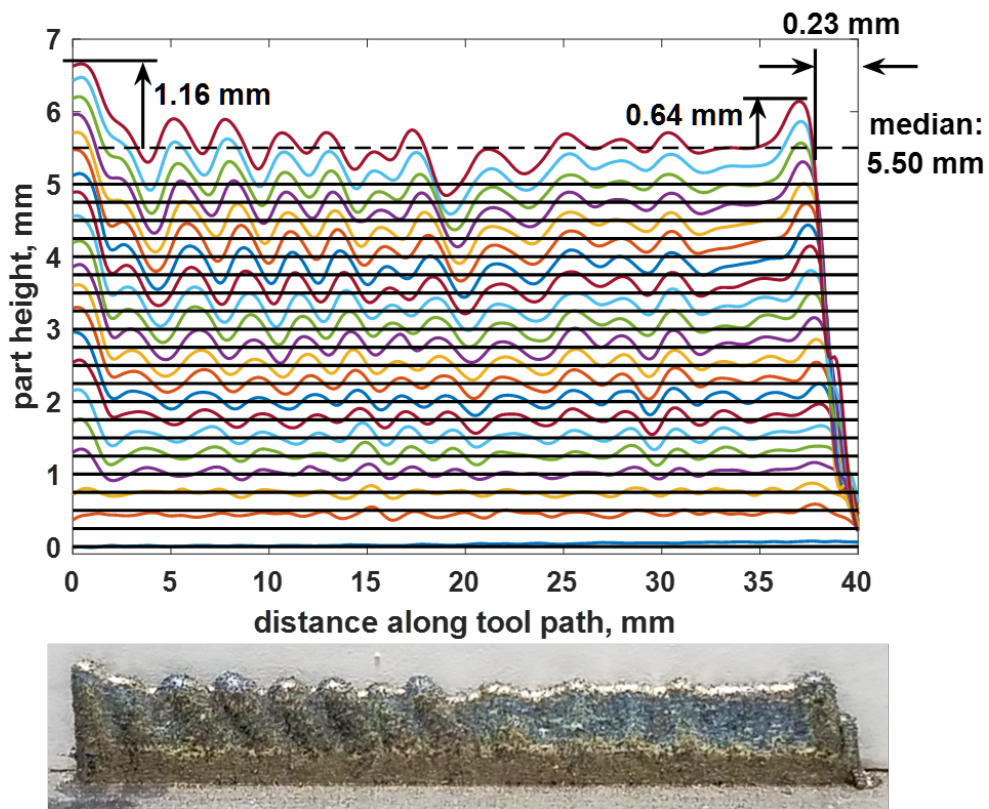
Figure 2. Open-loop wall.

the part edge at 40 mm shows that the open-loop process is unable to deposit the full length of the desired path. As layer increases, less of the desired path length is deposited and the final layer comes up about 2.5 mm short of the full length. This phenomenon was also observed on thin walls in [14]. Due to the lack of deposition at the right edge, the mean final height is skewed; thus the final height is better represented by the median rather than the mean. The median of the final height is 5.50 mm, which corresponds to a DC error of 0.50 mm. Lastly, there is overbuild at both ends of the wall, which protrudes 1.2 mm above the median height at the left edge and 0.6 mm at the right edge. This is not due to machine acceleration or deceleration at the ends because the lead-in motions allow the nozzle to maintain nominal speed prior to turning on the laser. Thus the melt pool itself must have dynamics that cause build-up at its initiation as well as termination. In the case of the closed-loop wall (Figure 4), the controller was able to prevent defects from propagating
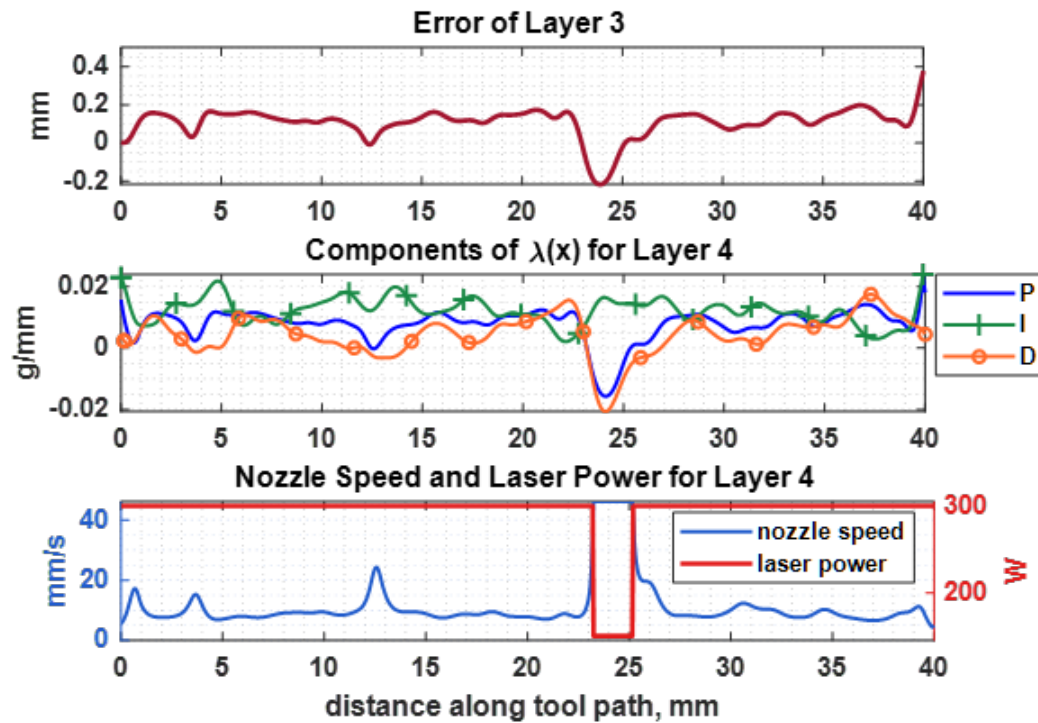
Figure 3. Signals after printing layer 3 of closed-loop wall.

and amplifying with layer. Specifically, an error was initiated on layer 3 at a distance of 24 mm along the tool path. This error, along with the velocity and laser command generated for the next layer, are shown in Figure 3. Since the error occurred suddenly on this layer, the proportional and derivative terms contributed the most to the speed correction for layer 4. Since the part overbuilt at this location, the controller generated a negative speed at that location and the aforementioned velocity and laser threshold were applied. The defect was eliminated within 2 layers. The median final height achieved by the controller was 4.88 mm, which corresponds to a height error of 0.12 mm. The wall length is also closer to the desired geometry, coming short by 0.7 mm of the desired 40 mm length. Overbuild at the ends is still observed in for the closed-loop case yet is not as pronounced, protruding only 0.38 mm above the mean final height.
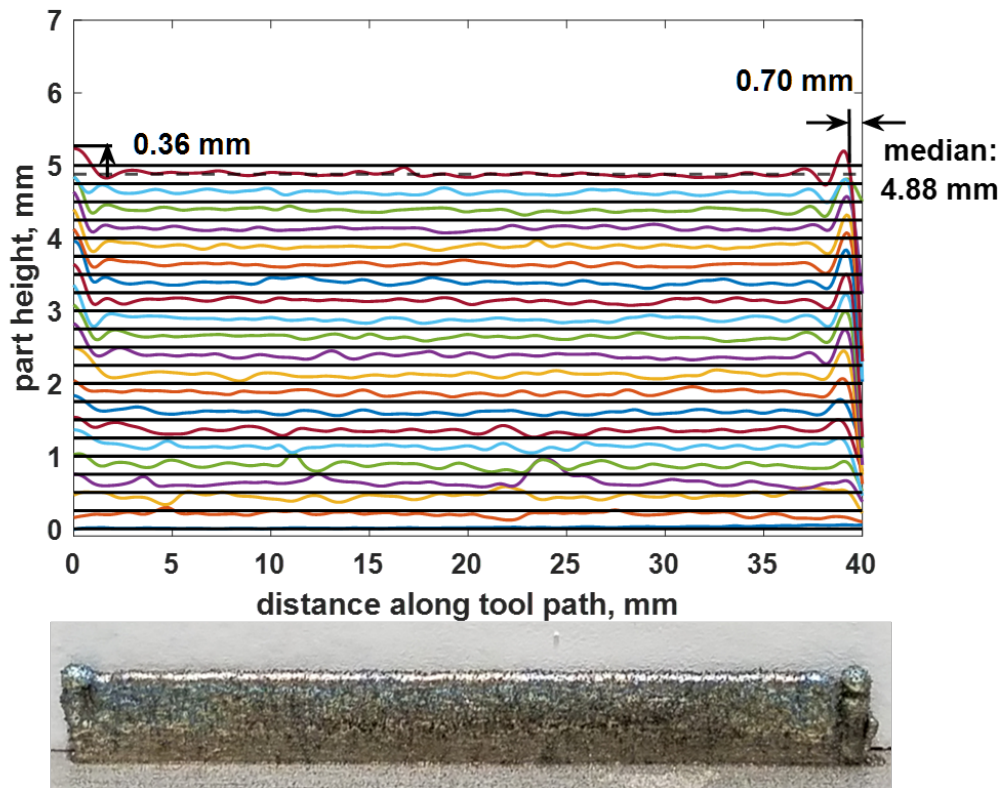
Figure 4. Closed-loop wall.

5.2. CLOSED CONTOUR PART

The matrix structure presented for closed paths in (22) was implemented on a cylindrical part. Like the thin wall part, the cylinder was designed to have 20 layers, although, with a diameter of 25 mm, the total tool path length was 78.5 mm.

As seen in Figures 5 and 6, the open-loop build displayed the same behavior as with the thin wall part: defect propagation and amplification; overbuild at the starting and ending points; and failure to deposit for the full length of the build, as seen by a deep depression at 77 mm. The final median height was 5.18 mm with the protrusions reaching a maximum of 1.18 mm above the median and the lowest recession lying 0.87 mm below the median.
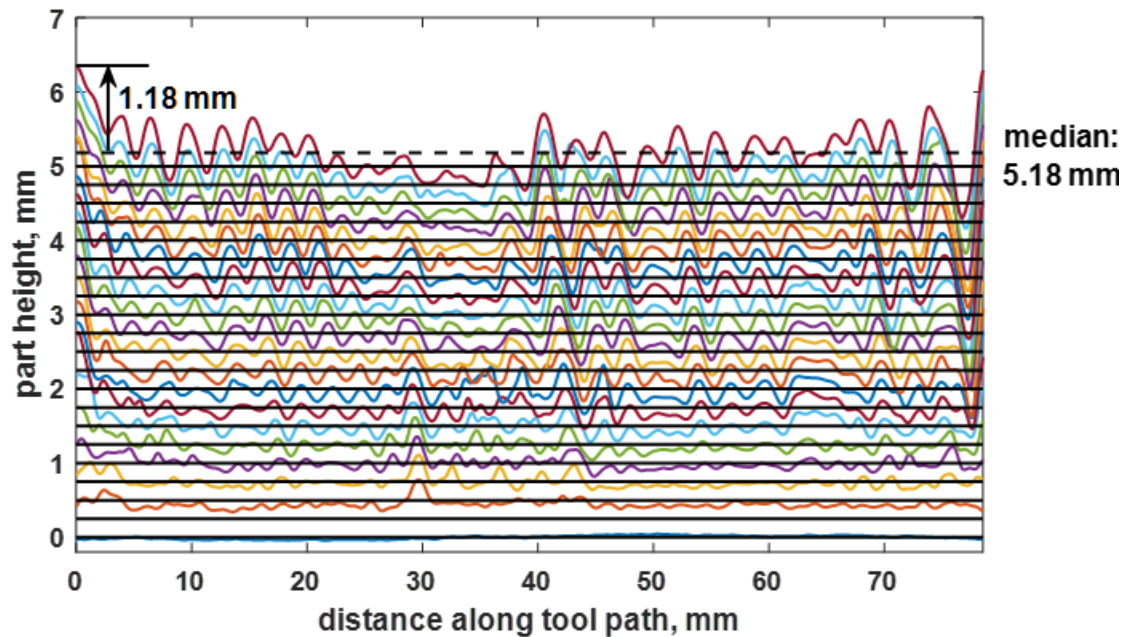
Figure 5. Open-loop cylinder heights.
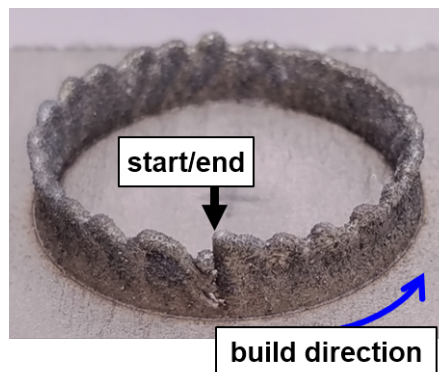
Figure 6. Open-loop cylinder.

On the other hand, the closed-loop build not only mitigated error propagation, but was able to maintain a continuous deposition across the starting and ending points. See Figures 7 and 8. Although the height defects occurred on layers 5 - 8 near 40 mm along the tool path, the controller successfully suppressed them. The junction does not exhibit protrusions, with the tallest point reaching only 0.17 mm above the median final height of 4.90 mm.
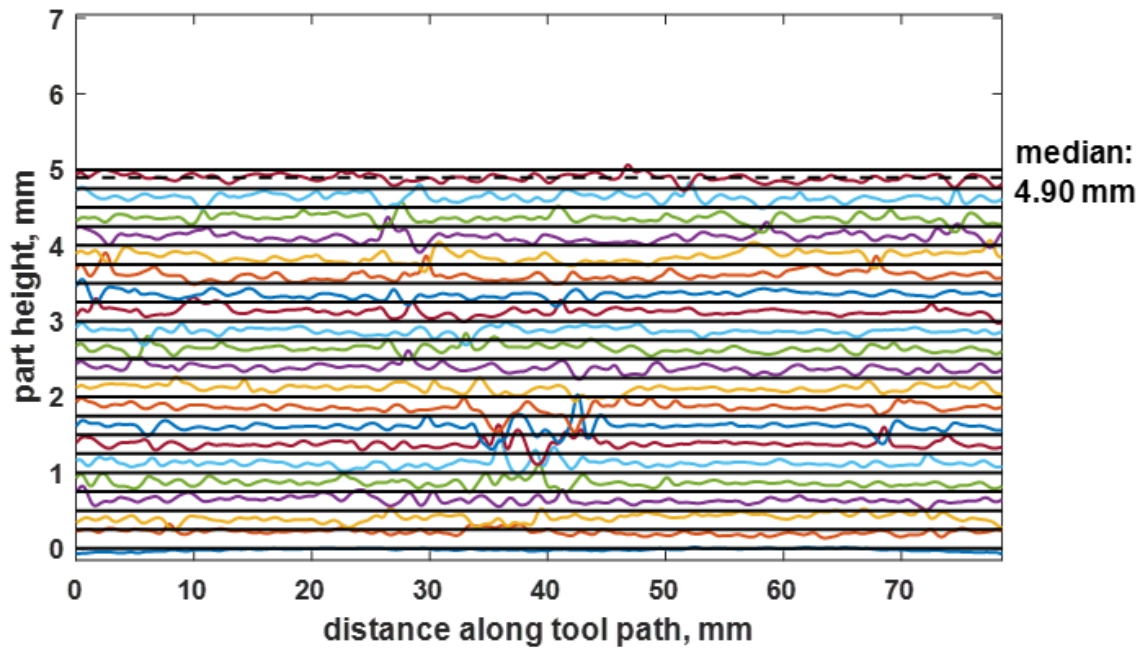
Figure 7. Closed-loop cylinder heights.
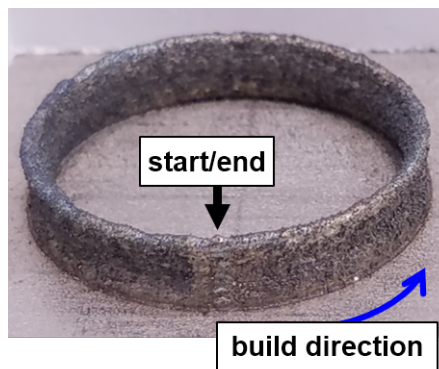
Figure 8. Closed-loop cylinder.

6. CONCLUSIONS

A quadratic optimal framework was developed for a generic repetitive process. Quadratic optimal control is a popular control structure that allows the designer to weight the trade-offs between error minimization and control effort. The optimal control solution resembled that of an iterative process, with the exception of a iteration-domain derivative

term that accounts for the iteration-to-iteration process dynamics. The control solution was formulated in the lifted representation of a dynamic system and thus could be directly implemented on an experimental platform.

The quadratic optimal solution was applied to control part height in laser metal deposition, a metal additive process which had been previously modeled as a repetitive process. The model describes the deposition height as a function of distance along the tool path and was originally formulated for a tool path that did not interact with itself. Here the matrix structure of the model (and thus controller) was modified to account for the interaction between beginning and end points that spatially coincide, such as the case for closed-contour toolpaths. In the future, it will be interesting to consider paths that interact at more than one point, such as the case for the raster paths commonly used for part infill in additive manufacturing.

Thin wall builds demonstrated the controller's ability to reduce overbuild at the end points - from 1.16 mm to 0.36 mm. Although the deposition passes included lead-in motions such that deposition did not occur during nozzle acceleration, overbuild was observed at the endpoints, which suggests that the process itself has start-up transients. When, in the case of the cylindrical builds, the start and end points coincided, the model matrix structure was modified to accounted for interaction of the endpoints. This allowed the controller to maintain the desired part height across the seam without any overbuild. For the controlled builds, the median final height differed from the desired height by 0.12 mm for the thin wall and 0.10 mm for the cylinder. This is approximately five times less than the open-loop median errors. The most important improvement achieved by the controller, however, was the suppression of ripple errors that otherwise propagate and amplify through LMD parts.

REFERENCES

[1] Zhang, X., Li, W., Chen, X., Cui, W., and Liou, F., 'Evaluation of component repair using direct metal deposition from scanned data,' The International Journal of Advanced Manufacturing Technology, 2018, **95**(9), pp. 3335–3348.

[2] Petrat, T., Graf, B., Gumenyuk, A., and Rethmeier, M., 'Laser metal deposition as repair technology for a gas turbine burner made of inconel 718,' Physics Procedia, 2016, **83**, pp. 761–768.

[3] Qi, H., Azer, M., and Singh, P., 'Adaptive toolpath deposition method for laser net shape manufacturing and repair of turbine compressor airfoils,' The International Journal of Advanced Manufacturing Technology, 2010, **48**(1-4), pp. 121–131.

[4] Hofmann, D. C., Roberts, S., Otis, R., Kolodziejska, J., Dillon, R. P., Suh, J.-o., Shapiro, A. A., Liu, Z.-K., and Borgonia, J.-P., 'Developing gradient metal alloys through radial deposition additive manufacturing,' Scientific reports, 2014, **4**(1), pp. 1–8.

[5] Soodi, M., Masood, S. H., and Brandt, M., 'Tensile strength of functionally graded and wafer layered structures produced by direct metal deposition,' Rapid Prototyping Journal, 2014.

[6] Wu, D., Liang, X., Li, Q., and Jiang, L., 'Laser rapid manufacturing of stainless steel 316l/inconel718 functionally graded materials: microstructure evolution and mechanical properties,' International Journal of Optics, 2010, **2010**.

[7] Zhu, G., Li, D., Zhang, A., Pi, G., and Tang, Y., 'The influence of standoff variations on the forming accuracy in laser direct metal deposition,' Rapid Prototyping Journal, 2011.

[8] Zekovic, S., Dwivedi, R., and Kovacevic, R., 'Numerical simulation and experimental investigation of gas–powder flow from radially symmetrical nozzles in laser-based direct metal deposition,' International Journal of Machine Tools and Manufacture, 2007, **47**(1), pp. 112–123.

[9] Manvatkar, V., De, A., and DebRoy, T., 'Heat transfer and material flow during laser assisted multi-layer additive manufacturing,' Journal of Applied Physics, 2014, **116**(12), p. 124905.

[10] Huang, Y., Leu, M. C., Mazumder, J., and Donmez, A., 'Additive manufacturing: current state, future potential, gaps and needs, and recommendations,' Journal of Manufacturing Science and Engineering, 2015, **137**(1).

[11] Tapia, G. and Elwany, A., 'A review on process monitoring and control in metal-based additive manufacturing,' Journal of Manufacturing Science and Engineering, 2014, **136**(6).

[12] Salehi, D. and Brandt, M., 'Melt pool temperature control using labview in nd: Yag laser blown powder cladding process,' The international journal of advanced manufacturing technology, 2006, **29**(3-4), pp. 273–278.

[13] Tang, L. and Landers, R. G., 'Melt pool temperature control for laser metal deposition processes—part ii: layer-to-layer temperature control,' Journal of manufacturing science and engineering, 2010, **132**(1).

[14] Bi, G., Gasser, A., Wissenbach, K., Drenker, A., and Poprawe, R., 'Characterization of the process control for the direct laser metallic powder deposition,' Surface and Coatings Technology, 2006, **201**(6), pp. 2676–2683.

[15] Toyserkani, E. and Khajepour, A., 'A mechatronics approach to laser powder deposition process,' Mechatronics, 2006, **16**(10), pp. 631–641.

[16] Ding, Y., Warton, J., and Kovacevic, R., 'Development of sensing and control system for robotized laser-based direct metal addition system,' Additive Manufacturing, 2016, **10**, pp. 24–35.

[17] Tang, L. and Landers, R. G., 'Layer-to-layer height control for laser metal deposition process,' Journal of Manufacturing Science and Engineering, 2011, **133**(2).

[18] Fathi, A., Khajepour, A., Toyserkani, E., and Durali, M., 'Clad height control in laser solid freeform fabrication using a feedforward pid controller,' The International Journal of Advanced Manufacturing Technology, 2007, **35**(3-4), pp. 280–292.

[19] Heralić, A., Christiansson, A.-K., Ottosson, M., and Lennartson, B., 'Increased stability in laser metal wire deposition through feedback from optical measurements,' Optics and Lasers in Engineering, 2010, **48**(4), pp. 478–485.

[20] Sammons, P. M., Gegel, M. L., Bristow, D. A., and Landers, R. G., 'Repetitive process control of additive manufacturing with application to laser metal deposition,' IEEE Transactions on Control Systems Technology, 2018, **27**(2), pp. 566–575.

[21] Gegel, M. L., Bristow, D. A., and Landers, R. G., 'A quadratic-optimal repetitive process controller for laser metal deposition,' in '2018 Annual American Control Conference (ACC),' IEEE, 2018 pp. 4446–4451.

[22] Sammons, P. M., Bristow, D. A., and Landers, R. G., 'Two-dimensional modeling and system identification of the laser metal deposition process,' Journal of Dynamic Systems, Measurement, and Control, 2019, **141**(2).

[23] Hoelzle, D. J. and Barton, K. L., 'On spatial iterative learning control via 2-d convolution: Stability analysis and computational efficiency,' IEEE Transactions on Control Systems Technology, 2015, **24**(4), pp. 1504–1512.

[24] Music, O. and Allwood, J. M., 'The use of spatial impulse responses to characterise flexible forming processes with mobile tools,' Journal of Materials Processing Technology, 2012, **212**(5), pp. 1139–1156.

[25] Wang, X., Bristow, D. A., and Landers, R. G., 'A switched adaptive model for layer-to-layer selective laser melting with varying laser paths,' in 'Dynamic Systems and Control Conference,' volume 84287, American Society of Mechanical Engineers, 2020 p. V002T24A002.

[26] Li, J., Wang, Q., Michaleris, P., and Reutzel, E. W., 'Model prediction for deposition height during a direct metal deposition process,' in '2017 American Control Conference (ACC),' IEEE, 2017 pp. 2188–2194.

[27] Ocelík, V., Eekma, M., Hemmati, I., and De Hosson, J. T. M., 'Elimination of start/stop defects in laser cladding,' Surface and Coatings Technology, 2012, **206**(8-9), pp. 2403–2409.

III. TWO-DIMENSIONAL LOOP SHAPING FOR LAYER-TO-LAYER CONTROL OF LASER METAL DEPOSITION

Michelle L. Gegel
Department of Mechanical & Aerospace Engineering
Missouri University of Science and Technology
Rolla, Missouri 65409–0050

Douglas A. Bristow
Department of Mechanical & Aerospace Engineering
Missouri University of Science and Technology
Rolla, Missouri 65409–0050
Tel: 573–341–6559
Email: dbristow@mst.edu

Robert G. Landers
Department of Aerospace & Mechanical Engineering
University of Notre Dame
Email: rlanders@nd.edu

ABSTRACT

A repetitive process is a system that experiences inputs in intervals, which are referred to as iterations, and exhibits dynamics within each iteration as well as dynamics that evolve with iteration. Limited work exists in control design for repetitive processes and traditionally the reference is assumed to be constant each iteration. One such process is a metal additive manufacturing process known as Laser Metal Deposition (LMD). In this process, metal parts are constructed in a layer-by-layer fashion where each layer can be modeled as an iteration of the repetitive process. Here, the output of the repetitive process is taken as the total part height and thus the reference will not be constant in this application, but will increase and evolve throughout the part build, particularly when fabricating parts with complex geometries. In this work, the norm-optimal repetitive process control that

was previously developed is extended to the case of varying references. Furthermore, a two-dimensional frequency-domain analysis of the norm-optimal control is used to select weighting parameters in order to track references that vary in two dimensions.

Keywords: metal additive manufacturing, multi-dimensional systems, frequency-domain control design

1. INTRODUCTION

Additive manufacturing (AM) offers the ability to produce parts with complex geometries while minimizing material usage and providing flexibility in design changes. In 2.5D additive processes, parts are constructed by a successive deposition of layers. Laser Metal Deposition (LMD) is a 2.5D additive manufacturing process where metal powder is delivered to a melt pool by a stream of inert gas. Compared with other metal additive processes, LMD has the distinct abilities to deposit features on existing parts, which is useful for high-value part repair [1, 2], and construct functionally graded parts [3, 4]. However, as with most AM processes, the dimensional accuracy and material quality of the resulting parts are highly dependent on user-selected process parameters and unknown variations in environmental factors. Important LMD process parameters include print speed, powder feed rate, laser power, and nozzle stand-off distance. In addition to these user-selected process parameters, thermal conditions affect the melt pool size and shape as well as the material properties of the final part. Much work has been done to model the thermophysical phenomenon, which are complex, yet deterministic. The deposition behavior is also influenced by non deterministic factors such as random fluctuations in the powder feed rate or shielding gas flow. Often defects that initiate on some layer, propagate through successive layers and amplify [5]. Due to the complexity of high-fidelity process models and the random nature of disturbances, in-process sensing and feedback control are needed to achieve consistent thermal conditions throughout the build and ensure dimensional accuracy [6].

Various types of controllers have been implemented in LMD. Easily measurable properties, such as melt pool size or temperature, are used as feedback and one or more process inputs are adjusted. Typically, laser power or print speed are chosen as the controlled inputs because they have larger bandwidths compared to powder feed rate. PID control was applied in [7, 8, 9] to control melt pool geometry by varying the laser power. In [9], different model parameters were identified for each layer, evidence of the time-varying thermal dynamics, and the PID gains were selected for each layer according to the changing process dynamics. These controllers produced a more uniform bead geometry for thin-wall parts. A similar result was achieved in [10], although temperature was measured rather than melt pool geometry. PID control using velocity as the controlled input variable was implemented in [11]. Predictive control has also been implemented. In [12], a model of melt pool temperature was used to optimize a cost function over future time steps, with constraints on the laser power input. This work was extended to include a switched control law where the laser shutter is turned off for overbuilt beads and the temperature MPC is active whenever the height is below the set point [13]. In [14], a Smith predictor was used to account for transport delays between the height sensor and processing zone. Tang and Landers estimated the model parameters after each layer and generated a control input for the next layer based on the updated model [15, 16].

The layer-by-layer nature of AM processes makes them well-suited for Iterative Learning Control (ILC) methods [17]. In this case, an iteration is taken to be the deposition of a single layer and control updates are calculated in between layers using information from the previous layers. Heralic et al. implemented ILC in [18] for wire-fed arc welding and demonstrated the controller on bosses printed with a sprial toolpath. Shi et al., [19], used ILC to control varying width depositions and [20] used ILC to adjust velocity each layer. More instances of ILC in AM appear for non-metal material processes, including 3D inkjet printing in [21] and [22].

Although ILC uses previous layer information in the control update law, the approach does not consider the affects of previous layers on the process itself. Here, LMD is modeled as a repetitive process, where where outputs from previous iterations are fed back as inputs to the current iteration. Laser metal deposition is best described as a repetitive process because the height and temperature of previous layers couple with the dynamics of the current layer. Previously, in [23], LMD was modeled as a repetitive process, having both in-layer and layer-to-layer dynamics. A controller was designed in [24] using a pole-placement approach and demonstrated on thin wall depositions. The present work modifies the repetitive process model from [23] and derives a novel control design.

Traditionally in ILC and Repetitive Process Control (RPC), the reference is assumed to be constant at each iteration. Likewise, most existing work in feedback control for metal AM seeks to track a constant set-point, whether melt pool temperature, melt pool size, or layer height. Some have employed controllers to track a reference that changes within the layer. In [11], PID was combined with model-inverse feedforward in order to track a sinusoidally varying bead height. A sliding mode controller was designed in [25] with an adaptive portion to track a spatially varying reference. In [26], multi-layer cladding was performed where the height varied along the pass, both as a ramp and a sinusoid. In all these cases, the reference varied within the layer. However, to create the complex parts for which AM is so desirable, non-planar slicing is required, which results in layer thicknesses that change both within the layer and from layer-to-layer [27]. This motivates our objective to track a reference that is varying in two dimensions: within the layer and from layer-to-layer. In [28], a repetitive process was considered where the 2D-varying reference had an analytical form and, thus, the internal model principle could be employed. In this work, we address the case where the reference is known, but does not have an analytical expression.

Our design approach combines norm-optimal control with loop shaping in a 2D frequency-domain. The norm-optimal control balances error rejection with the aggressiveness of control actions and the solution contains weighting functions that are used as design

parameters. Loop shaping is an effective design technique when the reference and distur-
bance occur in a different frequency band than the noise. In [29], robustness and steady-state
error specifications were related to the choice of weights in an ILC-LQR forumlation. This
resulted in loop-shaping over the spatial frequency domain and was combined with ILC.
Here we have frequency content in both the spatial and iteration domains. The sensitivity
of the error to the reference is a 2D transfer function, on which we impose an upper bound
for the region of frequencies desired to track. This results in a condition on the choice of
weights in the optimal formulation to achieve the desired 2D frequency-domain specifica-
tion. This approach was first presented in [30]. Here the control design was modified to
improve robustness and experimental results are included. Section II provides background
on the repetitive process model and motivates this investigation into 2D varying references.
The control design is developed in Section III and a design example is presented, followed
by experimental results in Section IV.

2. BACKGROUND

2.1. PROCESS MODEL

A repetitive process model for LMD was introduced in [23, 24]. The model describes
the morphology of a deposited bead in two dimensions: 1. along the build path, represented
by the independent variable x, and 2. at each layer, represented by the discrete variable
j. The model relates commanded inputs, such as the z-increment between layers and the
nozzle speed, to the bead height, while also incorporating the effect of previous layers. To
represent the model in a two-dimensional frequency domain, the spatial variable, x, can be
transformed into frequency domain using the bi-lateral Laplace transform. The layer index
j can also be transformed into a discrete frequency domain using the w-transform:

$$E(w) = \sum_{j=0}^{\infty} e(j)w^{-j}, \tag{1}$$
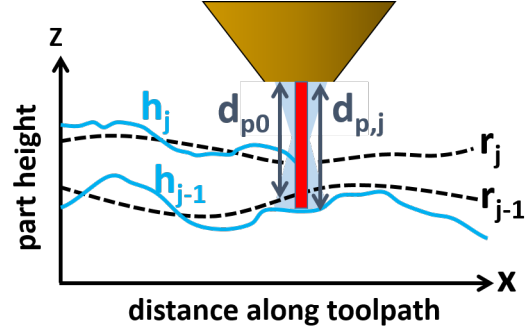
Figure 1. Diagram of variable designations.

where w^{-1} is a unit delay operator.

Here, the control development will begin with the error dynamics which have been transformed into the s-domain.

$$e_j(s) = A(s)e_{j-1}(s) + B(s)\lambda_j(s) + C(s,w)r_j(s) + d(s). \tag{2}$$

The signals e_j and e_{j-1} are height errors for the jth and $j - 1^{\text{th}}$ layers respectively (mm), λ_j is the process input and represents the spatial mass flow rate (g/mm), r_j is the reference height for the part j^{th} layer (mm) and $d(s)$ is a layer-invariant disturbance (mm). The functions $A(s)$ and $B(s)$ are spatial filters on the error and input respectively while $C(s,w)$ is a filter with both spatial and layer-domain dynamics. In a common abuse of notation, the expression $C(s,w)r_j$ is used to denote the inverse-w-transform of $C(s,w)r(s,w)$. The reader is referred to [30] for details regarding the model functions $A(s)$, $B(s)$ and $C(s,w)$.

2.2. 2D VARYING REFERENCES IN LMD

A major selling point for metal additive manufacturing is the ability to produce parts with complex geometries. When fabricating such parts, non-planar slicing is often necessary or preferred to achieve improved surface finish or mechanical properties in the

part. With non-planar slicing, each layer will have variation in layer thickness throughout the layer. However, it is the evolution of layer thickness *with layer* that results in a reference height that varies in two dimensions. An example of such a part is shown in Figure 2.
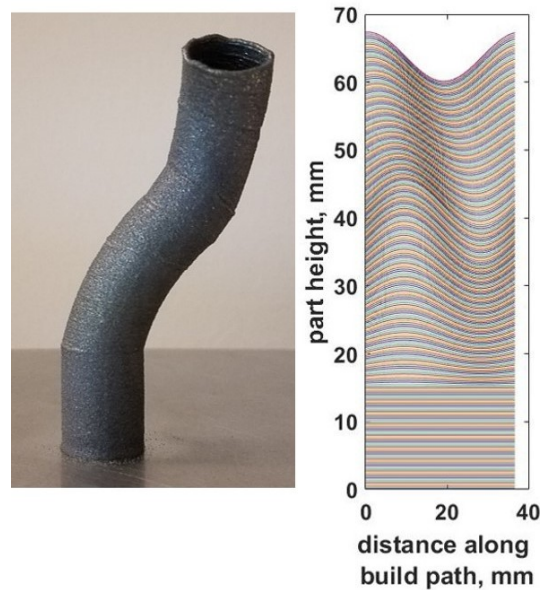
Figure 2. Cylindrical part with 2D varying reference.

3. CONTROL DESIGN

3.1. NORM-OPTIMAL CONTROL SOLUTION

In [31], norm-optimal control was developed for a repetitive process in lifted form. The norm-optimal solution can also be formulated with the model in spatial frequency domain. Consider the cost function,

$$J(s) = \overline{e_j(s)}Q(s)e_j(s) \ldots$$
$$+ (\overline{\lambda_j(s) - \lambda_{j-1}(s)})R(s)(\lambda_j(s) - \lambda_{j-1}(s)), \tag{3}$$

where $Q(s)$ $(1/mm^2)$ and $R(s)$ (mm^2/g^2) are positive definite, scalar functions selected by the designer and $\overline{(\cdot)}$ denotes the complex conjugate. For conciseness, we will drop the argument (s) from the signals. Since the signals e_j and d are not known prior to depositing the jth layer, the model equation in (2) is used to express those signals in terms of previous layer quantities. Then the norm-optimal solution is

$$\lambda_j = L_e e_{j-1} + L_\lambda \lambda_{j-1} \ldots$$
$$+ L_{de}(e_{j-1} - e_{j-2}) + L_r C(s, w)(r_j - r_{j-1}) \tag{4}$$

where

$$L_e = -(\overline{B}QB + R)^{-1}\overline{B}Q$$
$$L_\lambda = (\overline{B}QB + R)^{-1}(\overline{B}QB + R) = I$$
$$L_{de} = -(\overline{B}QB + R)^{-1}\overline{B}QA$$
$$L_r = -(\overline{B}QB + R)^{-1}\overline{B}Q. \tag{5}$$

Note that this solution allows the reference to change with iteration. If the reference does not change with iteration, as is often the case for repetitive processes, then the feed-forward term of this controller is zero. For the LMD process in particular, the reference was defined to be the *total* part height after each layer and thus the reference changes each iteration. However, if the part reference changes by a constant amount every layer, i.e. if the layer thickness does not change with layer, then the LMD model yields $C(s, w)r_j = C(s, w)r_{j-1}$ and the feed-forward term of this controller is zero. Thus, in LMD, the feed-forward term in the optimal solution only contributes for parts whose layer thicknesses changes with layer.
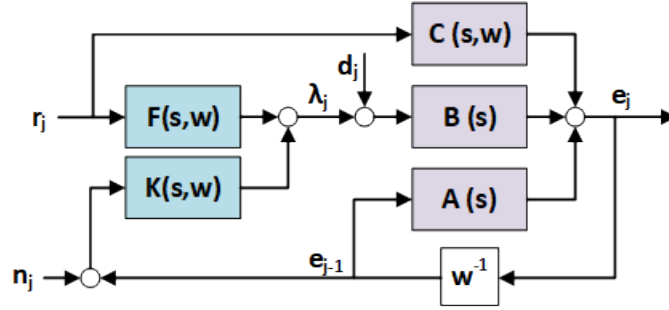
Figure 3. Block diagram.

3.2. 2D LOOP SHAPING

Consider the generic repetitive process shown in Figure 3 where the controller has a feedback component, $K(s, w)$, as well as a feedforward component, $F(s, w)$. The error is affected by the reference, disturbance and noise signals according to

$$
\begin{aligned}
e(s, w) = {} & \frac{B(s)F(s, w) + C(s, w)}{1 - (A(s) + B(s)K(s, w))w^{-1}} r(s, w) \\
& \cdots + \frac{B(s)}{1 - (A(s) + B(s)K(s, w))w^{-1}} d(s, w) \\
& \cdots + \frac{B(s)K(s, w)}{1 - (A(s) + B(s)K(s, w))w^{-1}} n(s, w) \\
= {} & S_r(s, w)r(s, w) + S_d(s, w)d(s, w) + S_n(s, w)n(s, w).
\end{aligned}
\tag{6}
$$

The designer is then faced with a question: How should $K(s, w)$ and $F(s, w)$ be selected? The norm-optimal solution presented earlier offers an option for these two-dimensional compensators.

$$
K(s, w) = \frac{-\overline{B}Q(1 + A - w^{-1}A)}{\overline{B}QB + R + S - w^{-1}(\overline{B}QB + R)}
\tag{7}
$$

$$
F(s, w) = \frac{-\overline{B}QC(s, w)}{\overline{B}QB + R + S - w^{-1}(\overline{B}QB + R)} \cdot \frac{w - 1}{w}.
\tag{8}
$$

Since the objective of this work is to track 2D-varying references, the design will focus on the sensitivity from the reference to the error, S_r. The 2D-varying reference is considered to have frequency content within a known region. Over this region, it is desired to bound the 2D transfer function $S_r(s, w)$.

$$|S_r(s_0, w_0)| = \left| \frac{e(s_0, w_0)}{r(s_0, w_)} \right| \leq \eta, \tag{9}$$

for all $s_0 \in [s_l, s_h]$ and $w_0 \in [w_l, w_h]$. The real, positive scalar η is a design parameter. Substituting (7) and (8) into (6) yields the sensitivity to the reference for the norm-optimal control solution.

$$S_r = \frac{\left[Rw(w-1) + Sw^2 \right] C(s, w)}{w^2 \overline{B} Q B + R(w-A)(w-1) + S(w-A)w} \tag{10}$$

In the literature, it is known that the weight on the control in the LQR formulation, here called S, provides robustness to model uncertainties. The weight on change in control, here called R, is most associated with convergence rate - larger penalties on the change in control adversely affect tracking performance. How large can the weight R be selected and still achieve some desired level of tracking performance? That is addressed by the following theorem.

Theorem:

Let M be a 2D region of complex numbers s and w, $Q(s) = 1$, $R(s)$ and $S(s)$ be positive definite functions of s and $\eta \in \mathbb{R}^+$. If

$$|R| \leq \frac{\eta \left| S(w-A)w + w^2 \overline{B} B \right| - |SC|}{|C(w-1)| + \eta |(w-A)(w-1)|} \tag{11}$$

holds for all $(s, w) \in M$, then it follows

$$|S_r(s, w)| \le \eta \tag{12}$$

for all $(s, w) \in M$.

Proof:

Starting with the theorem's condition, we can prove its conclusion.

$$|R| \le \frac{\eta \left| S(w - A)w + w^2 \overline{B}B \right| - |SC|}{|C(w - 1)| + \eta |(w - A)(w - 1)|}$$

$$|R| |C(w - 1)| + \eta |(w - A)(w - 1)| \le \eta \left| S(w - A)w + w^2 \overline{B}B \right| - |SC|$$

$$|R| |C(w - 1)| + |SC| \le \eta \left| S(w - A)w + w^2 \overline{B}B \right| - \eta |R| |(w - A)(w - 1)|$$

$$\left| RCw(w - 1) + SCw^2 \right| \le \eta \left| S(w - A)w + w^2 \overline{B}B + R(w - A)(w - 1) \right|$$

$$\frac{\left| Rw(w - 1) + Sw^2 \right| |C|}{\left| w^2 \overline{B}B + R(w - A)(w - 1) + S(w - A)w \right|} \le \eta \tag{13}$$

The proof makes use of triangle inequalities such that the final result is conservative. Thus (11) is a sufficient, though not necessary, condition for (12).

3.3. DESIGN EXAMPLE

As a case of a simple 2D-varying reference, consider a thin wall part with a reference according to

$$r_j(x) = (0.25 \text{ mm}) \sin(2\pi F_x x + 2\pi F_j j) + (0.25 \text{ mm}) j. \tag{14}$$
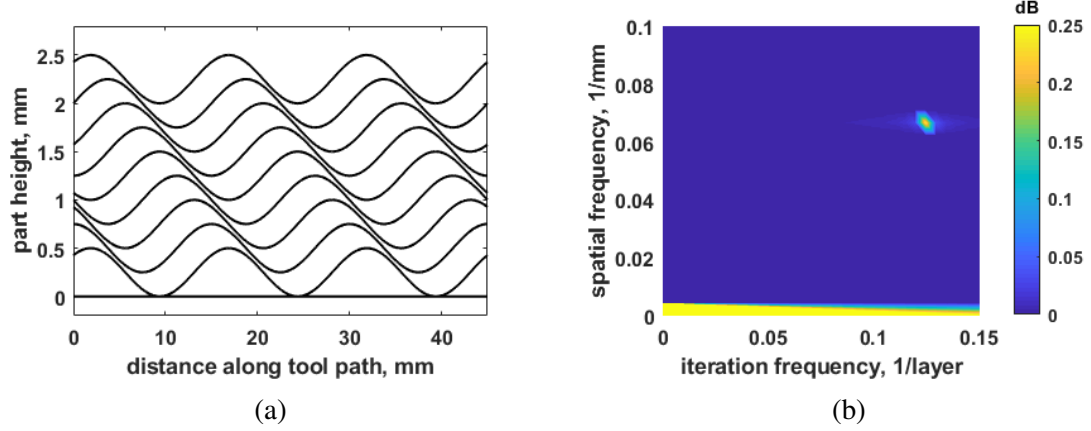
Figure 4. Example wavy wall height reference in (a) spatial and layer domain and (b) 2D frequency domain.

Although we have an analytical expression of the 2D reference for this example, note that the design method does not require an equation for the reference but only knowledge of its bandwidth. For this example, the spatial frequency, F_x, is chosen to be 0.067 mm^{-1} which corresponds to a 15 mm period, and the iteration frequency is chosen as 0.125 layer^{-1} which corresponds to a feature that repeats every 8$^{\text{th}}$ layer. The reference is shown in the spatial and layer domains in Figure 4a and in the 2D frequency domain in Figure 4b.

As a design choice, the desired bound on S_r will be selected as $\eta = 0.25$, which corresponds to an error magnitude of 0.063 mm for the reference in (14). The penalty on control magnitude, $S(s)$, was selected to be zero. With this choice of η and $S(s)$ and selecting the region M as $F_x \in [0, 0.067]$ mm^{-1} and $F_j \in [0, 0.125]$ layer^{-1}, the upper bound on $|R(s)|$ given by (11) was evaluated numerically. The bound's minimum over the region of interest was found to be 29.1 mm^2/g^2. To meet the condition, $R(s)$ was selected as 17.1 mm^2/g^2. To verify the performance achieved, Figure shows contours of the surface S_r after selecting R according to the design method. The blue line is the contour that corresponds to the selected η and the pink dashed line outlines the region of interest. The contours of S_r within the region of interest are seen to be below the design specification.
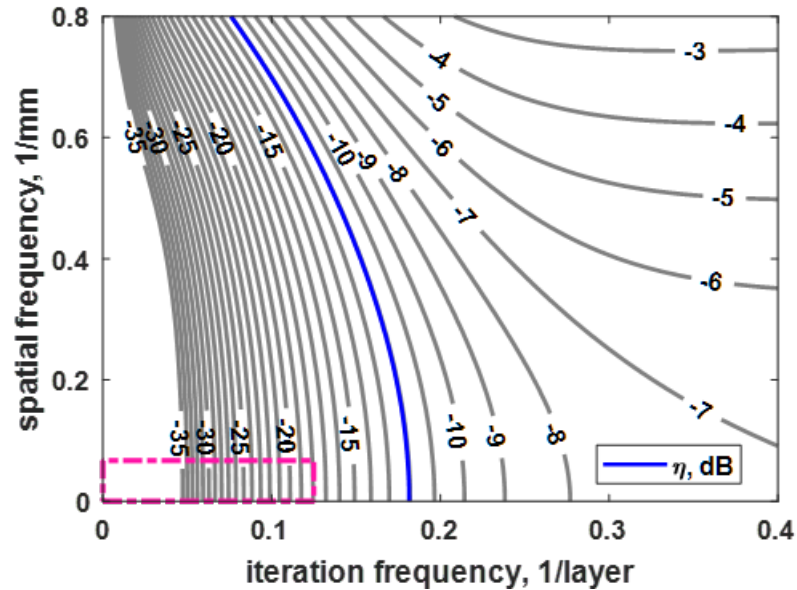
Figure 5. Contours of S_r

4. EXPERIMENTAL RESULTS

4.1. EXPERIMENTAL SET-UP

The experiments were performed on a 5-axis LMD machine at Missouri S&T. This system includes an Optomec LENS Print Engine (LPE), an Optomec powder feeder, a 1kW ytterbium laser (IPG YLR-1000-MM-WC-Y14), which are all centrally controlled by a National Instruments PXI (PXI-8186) running LabVIEW Real-Time 17.0.0. Feedback measurements are obtained between layers using a laser line scanner (Keyence LJ-V7200), which has a resolution of 0.001 mm in the vertical direction and 0.1 mm along the laser line. The repeatability on cladded surfaces has been found to be 0.006 mm. The measurements are triggered from the x-axis encoder, ensuring precise spacing between measurements and correlation between the scan data and machine toolpath. The encoder resolution is 0.25 μm and the scanner is set to trigger every 0.1 mm. Measurement noise is filtered using a low-pass Gaussian filter with a cut-off length of 1.2 mm, approximately equal to the melt pool length. The material used is 316L stainless steel, with a diameter range 53 - 150 μm.

The model and process parameters for the experiments are given in the appendix, Tables A.1 and A.2. The control input given by (4) is calculated using the lifted representation, and converted to the velocity profile

$$v_j(x) = \frac{\lambda_0 v_0}{\lambda_j(x)} \tag{15}$$

where v_0 is the nominal velocity (mm/s) and λ_0 is the nominal spatial mass flow rate (g/mm). Since the motion control for the machine is position-based, the velocity profile is converted to a position profile in time, which is fed point-by-point as reference to the motion controller. The motion controller ran in LabVIEW Real-Time at a rate of 5,000 Hz.
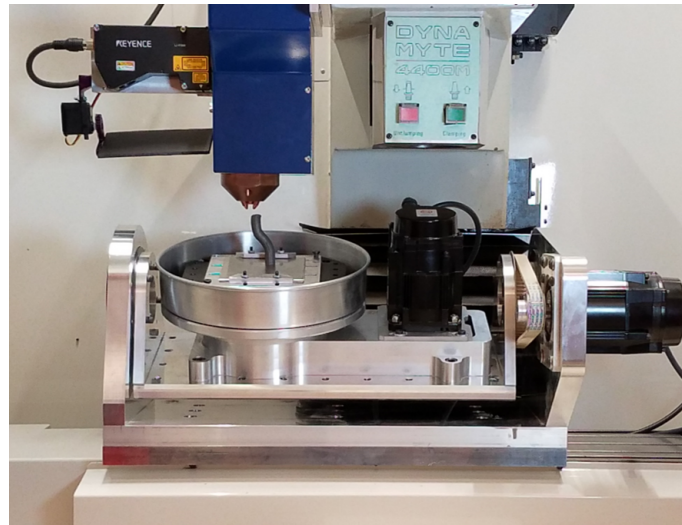
Figure 6. LENS machine at Missouri S&T.

4.2. WAVY WALL BUILD

The wavy wall part introduced previously in the design example was fabricated in experiment. The nozzle translated in the z-direction along each pass such that a constant height above the previous layer's reference was maintained. The height measured after each layer is shown in Figure 7 as colored lines and the reference for the final layer is shown in black.
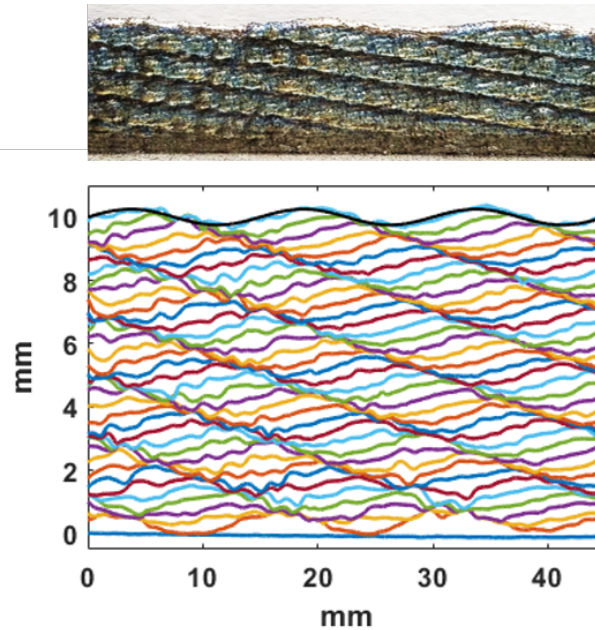
Figure 7. Wavy wall build.

The error component at the reference frequency, $F_x = 0.067$ mm^{-1} and $F_j = 0.125$ layer^{-1}, was 0.079 mm. Since the reference sinusoid has a magnitude of 0.25 mm, this error magnitude corresponds to $\eta = 0.32$. The higher-frequency undulations observed during this build were later mitigated by tuning the parameter S.

4.3. 5-AXIS PART

After tuning the parameter S, a suitable value to improve robustness was found to be $S = 0.5$. Then the controller with weights $Q(s) = 1$, $R(s) = 0.25$ and $S(s) = 0.5$ was applied to the complex part geometry shown in Figure 11. The height reference for this part was generated using non-planar slicing. When the reference height along the toolpath is unwrapped, it is observed to be a 2D-varying height reference (Figure 8). The part was fabricated using 5-axis motion so that, each layer, the top surface of the part was oriented level with respect to the machine's x-y plane. The part had 200 layers.
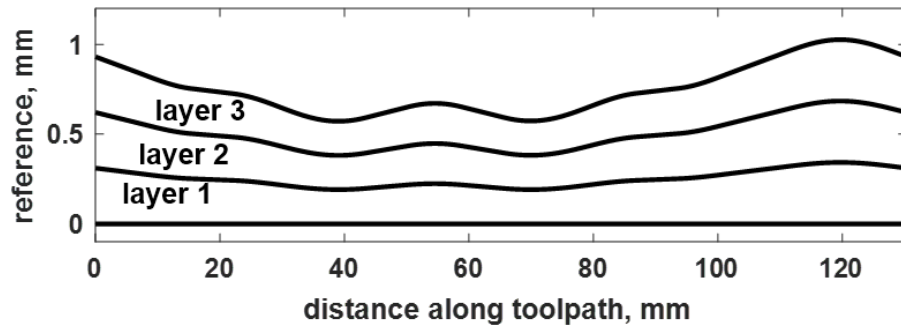
Figure 8. Reference height for first three layers of 5-axis part.

For the open-loop build, the commanded nozzle speed inversely proportional to the desired layer thickness. Merely 20 layers were deposited before the part was deemed irrecoverable and the build aborted, see Figure 9. By contrast, the closed-loop part completed the entire 200 layers successfully and the final part is shown in Figure 11. For some reason unknown to the authors, a notable height error occurred on layer 104. Approximately half way through the toolpath, the deposition ceased altogether. Such an error could be due to a momentary clog in the powder feed system or a rare glitch in the motion generation software. Regardless of the source of the error, the controller was able to recover within 4 layers of the defect's occurrence.

Figure 9. Open-loop 5-axis part, 20 layers.
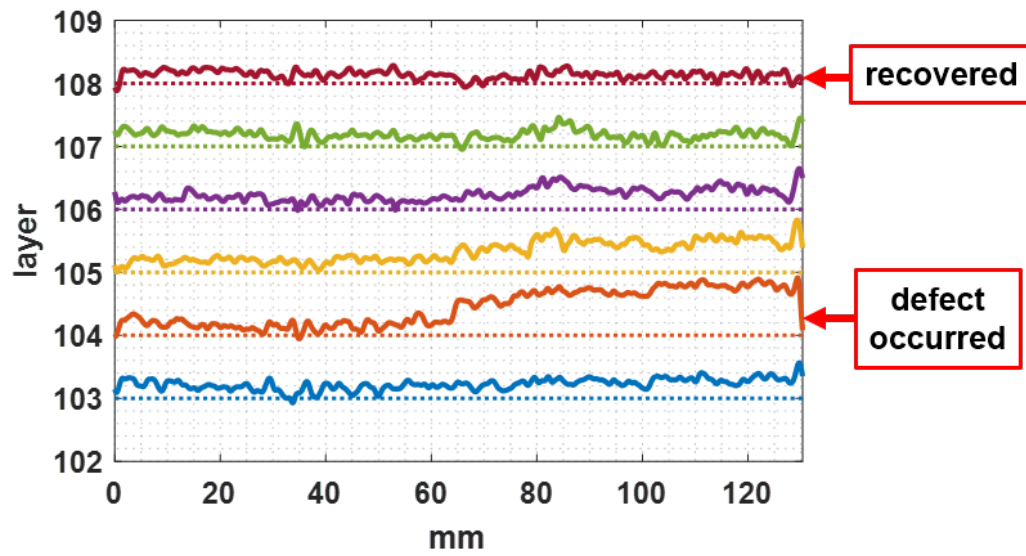
Figure 10. Error for layers 103-108.
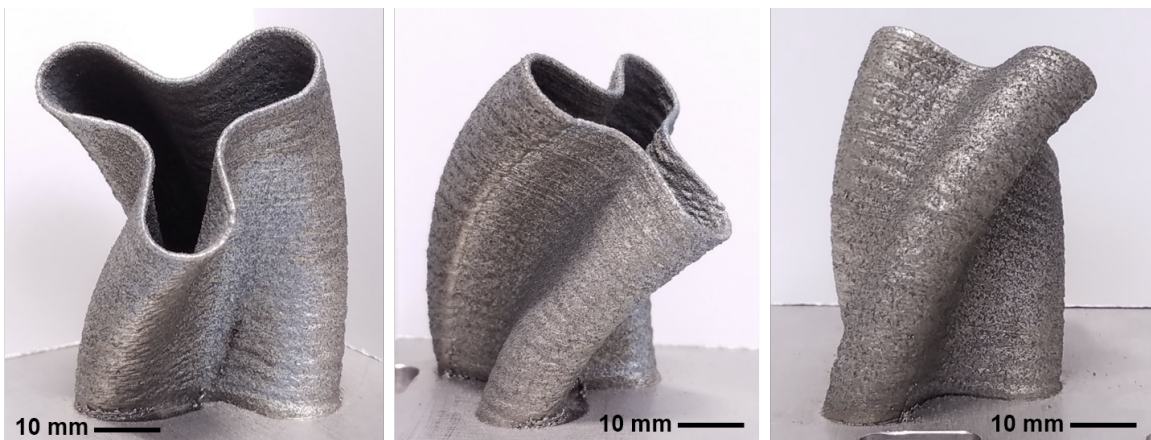
Figure 11. Closed-loop 5-axis part, 200 layers.

5. SUMMARY AND CONCLUSIONS

Analysis of the controller and system in a 2D frequency domain facilitated a 2D loop shaping approach. The objective of the controller was to track references within a user-specified 2D bandwidth. By extending norm-optimal RPC to the case of iteration-varying references, the flexibility of LQR control could be combined with consideration for the 2D tracking performance. A condition was developed on the choice of the norm-optimal

weighting parameter $R(s)$ that guaranteed tracking performance to the level specified by the designer. It was found that the parameter S was needed for robustness to model uncertainty, as the first experimental build showed errors at frequencies greater than the designed tracking bandwidth. After tuning the parameter S, the controller was implemented on a 5-axis part and was seen to track the desired reference while also rejecting disturbances.

APPENDIX

The model transfer functions $A(s)$, $B(s)$ and $C(s, w)$, in terms of model functions presented in [24] are

$$A(s) = F_r(s) - \kappa_2 F_s(s) \tag{1}$$

$$B(s) = -\kappa 1 F_s(s) \tag{2}$$

$$C(s, w) = 1 - w^{-1} F_r(s) \tag{3}$$

where

$$F_s(s) = \frac{2e^{-s\delta}(1 - (1 + ls)e^{-sl})}{l^2 s^2} \tag{4}$$

$$F_r(s) = \frac{-2 + e^{-sl_r} + e^{sl_r}}{l_r^2 s^2}. \tag{5}$$

The model parameters for the experiments presented here are given in Table A.1. The process parameters are given in Table A.2.

Table A.1. Model Parameters

Parameter	Symbol	Value	
		Wavy Wall	5-axis Part
melt pool length, mm	l	1.01	1.01
melt pool shift, mm	δ	-0.66	-0.91
remelt length, mm	l_r	0.52	0.52
melt pool width, mm	b_0	0.8	0.8
max powder catchment	α_{max}	0.061	0.066
catchment width, mm	α_{width}	3.15	3.37
powder focal distance, mm	d_{max}	8.02	8.65
nominal speed, mm/s	v_0	8.5	8.5
nominal mass addition, g/mm	λ_0	0.0263	0.0280

Table A.2. Process Parameters

Parameter	Value	
	Wavy Wall	5-axis Part
laser power, W	300	300
powder feed rate, g/s	0.22	0.24
initial stand-off distance, mm	7.5	8
z-increment, mm	0.25	0.25

REFERENCES

[1] Pinkerton, A., Wang, W., and Li, L., 'Component repair using laser direct metal deposition,' Proceedings of the Institution of Mechanical Engineers, Part B: Journal of Engineering Manufacture, 2008, **222**(7), pp. 827–836.

[2] Zhang, X., Li, W., and Liou, F., 'Damage detection and reconstruction algorithm in repairing compressor blade by direct metal deposition,' The International Journal of Advanced Manufacturing Technology, 2018, **95**(5), pp. 2393–2404.

[3] Hofmann, D. C., Roberts, S., Otis, R., Kolodziejska, J., Dillon, R. P., Suh, J.-o., Shapiro, A. A., Liu, Z.-K., and Borgonia, J.-P., 'Developing gradient metal alloys through radial deposition additive manufacturing,' Scientific reports, 2014, **4**(1), pp. 1–8.

[4] Domack, M. and Baughman, J., 'Development of nickel-titanium graded composition components,' Rapid Prototyping Journal, 2005.

[5] Liu, J. and Li, L., 'In-time motion adjustment in laser cladding manufacturing process for improving dimensional accuracy and surface finish of the formed part,' Optics & Laser Technology, 2004, **36**(6), pp. 477–483.

[6] Everton, S. K., Hirsch, M., Stravroulakis, P., Leach, R. K., and Clare, A. T., 'Review of in-situ process monitoring and in-situ metrology for metal additive manufacturing,' Materials & Design, 2016, **95**, pp. 431–445.

[7] Toyserkani, E. and Khajepour, A., 'A mechatronics approach to laser powder deposition process,' Mechatronics, 2006, **16**(10), pp. 631–641.

[8] Ding, Y., Warton, J., and Kovacevic, R., 'Development of sensing and control system for robotized laser-based direct metal addition system,' Additive Manufacturing, 2016, **10**, pp. 24–35.

[9] Akbari, M. and Kovacevic, R., 'Closed loop control of melt pool width in robotized laser powder–directed energy deposition process,' The International Journal of Advanced Manufacturing Technology, 2019, **104**(5), pp. 2887–2898.

[10] Bi, G., Schürmann, B., Gasser, A., Wissenbach, K., and Poprawe, R., 'Development and qualification of a novel laser-cladding head with integrated sensors,' International Journal of Machine Tools and Manufacture, 2007, **47**(3-4), pp. 555–561.

[11] Fathi, A., Khajepour, A., Toyserkani, E., and Durali, M., 'Clad height control in laser solid freeform fabrication using a feedforward pid controller,' The International Journal of Advanced Manufacturing Technology, 2007, **35**(3-4), pp. 280–292.

[12] Song, L. and Mazumder, J., 'Feedback control of melt pool temperature during laser cladding process,' IEEE Transactions on control systems technology, 2010, **19**(6), pp. 1349–1356.

[13] Song, L., Bagavath-Singh, V., Dutta, B., and Mazumder, J., 'Control of melt pool temperature and deposition height during direct metal deposition process,' The International Journal of Advanced Manufacturing Technology, 2012, **58**(1), pp. 247–256.

[14] Doumanidis, C. and Kwak, Y.-M., 'Geometry modeling and control by infrared and laser sensing in thermal manufacturing with material deposition,' J. Manuf. Sci. Eng., 2001, **123**(1), pp. 45–52.

[15] Tang, L. and Landers, R. G., 'Melt pool temperature control for laser metal deposition processes—part ii: layer-to-layer temperature control,' Journal of manufacturing science and engineering, 2010, **132**(1).

[16] Tang, L. and Landers, R. G., 'Layer-to-layer height control for laser metal deposition process,' Journal of Manufacturing Science and Engineering, 2011, **133**(2).

[17] Bristow, D. A., Tharayil, M., and Alleyne, A. G., 'A survey of iterative learning control,' IEEE control systems magazine, 2006, **26**(3), pp. 96–114.

[18] Heralić, A., Christiansson, A.-K., and Lennartson, B., 'Height control of laser metal-wire deposition based on iterative learning control and 3d scanning,' Optics and lasers in engineering, 2012, **50**(9), pp. 1230–1241.

[19] Shi, T., Lu, B., Shen, T., Zhang, R., Shi, S., and Fu, G., 'Closed-loop control of variable width deposition in laser metal deposition,' The International Journal of Advanced Manufacturing Technology, 2018, **97**(9), pp. 4167–4178.

[20] Das, A., Mukherjee, S., Giri, S. K., and Lohar, A., 'An improved learning based multilayer height control strategy in lmd process,' in '2017 14th IEEE India Council International Conference (INDICON),' IEEE, 2017 pp. 1–6.

[21] Lu, L., Zheng, J., and Mishra, S., 'A layer-to-layer model and feedback control of ink-jet 3-d printing,' IEEE/ASME Transactions on Mechatronics, 2014, **20**(3), pp. 1056–1068.

[22] Lim, I., Hoelzle, D. J., and Barton, K. L., 'A multi-objective iterative learning control approach for additive manufacturing applications,' Control Engineering Practice, 2017, **64**, pp. 74–87.

[23] Sammons, P. M., Bristow, D. A., and Landers, R. G., 'Two-dimensional modeling and system identification of the laser metal deposition process,' Journal of Dynamic Systems, Measurement, and Control, 2019, **141**(2).

[24] Sammons, P. M., Gegel, M. L., Bristow, D. A., and Landers, R. G., 'Repetitive process control of additive manufacturing with application to laser metal deposition,' IEEE Transactions on Control Systems Technology, 2018, **27**(2), pp. 566–575.

[25] Zeinali, M. and Khajepour, A., 'Height control in laser cladding using adaptive sliding mode technique: theory and experiment,' Journal of manufacturing science and engineering, 2010, **132**(4).

[26] Fathi, A., Khajepour, A., Durali, M., and Toyserkani, E., 'Geometry control of the deposited layer in a nonplanar laser cladding process using a variable structure controller,' Journal of manufacturing science and engineering, 2008, **130**(3).

[27] Xin, B., Zhou, X., and Gong, Y., 'Surface based variable thickness slicing modeling for laser metal deposition,' The International Journal of Advanced Manufacturing Technology, 2020, **107**(1), pp. 463–474.

[28] Omer, E.-S. A. and Moore, K. L., 'Norm-optimal control of time-varying discrete repetitive processes with iteration-varying reference inputs,' in 'The 2011 International Workshop on Multidimensional (nD) Systems,' IEEE, 2011 pp. 1–6.

[29] Gorinevsky, D., 'Loop shaping for iterative control of batch processes,' IEEE Control Systems Magazine, 2002, **22**(6), pp. 55–65.

[30] Gegel, M. L., Bristow, D. A., and Landers, R. G., 'A loop-shaping method for frequency-based design of layer-to-layer control for laser metal deposition,' in '2020 American Control Conference (ACC),' IEEE, 2020 pp. 487–491.

[31] Gegel, M. L., Bristow, D. A., and Landers, R. G., 'A quadratic-optimal repetitive process controller for laser metal deposition,' in '2018 Annual American Control Conference (ACC),' IEEE, 2018 pp. 4446–4451.

SECTION

2. CONCLUSIONS

The bead morphology in Direct Energy Deposition is best described mathematically as a repetitive process, because that framework captures the phenomenon of layer-to-layer defect propagation. The initiation and amplification of defects with layer was observed in the open-loop experimental builds. Although it is possible that the open-loop behavior could be improved by adjusting the process parameters, nonetheless, under the same process conditions that produced a poor open-loop part, the layer-to-layer controller prevented defects from persisting in subsequent layers.

There are limited design techniques for repetitive process controllers. Thus, the extension of the flexible and popular norm-optimal control formulation to the class of repetitive processes is a novel and useful contribution. The norm-optimal formulation allows the designer to quantify the desired trade-offs between tracking, convergence and robustness to model uncertainties. In practice, the level of required robustness was determined by tuning and experiments. A properly-tuned layer-to-layer feedback controller was found to effectively reject disturbances and significantly improve geometric accuracy in DED parts.

The norm-optimal control formulation was then extended to accommodate references with variations in both the spatial and layer domains. In this application, such a reference could come from a part with complex geometry. Analyzing the system and reference signals in a two-dimensional frequency domain lead to a loop-shaping approach to designing the weight parameters of the norm-optimal formulation. This approach does not require an analytical expression for the reference but merely that its bandwidth is known, both with respect to the spatial variable and with respect to the layer domain.

Another contribution of this work was the construction of an open-architecture DED system. The system is capable of 5-axis motion generation, which allows for construction of complex part geometries. A laser line scanner measurement device has been integrated with the DED system to provide layer-to-layer feedback. Height measurements can be extracted from the scan along any arbitrary tool path and any control algorithm that generates nozzle speed trajectory can be implemented.

One avenue of future work would be to extend the model from a single spatial variable - distance along toolpath - to two spatial variables, x and y and to account for interactions of the path with itself. For example, in the case of the closed-contour path considered in paper II, the tool path interacted with it self at a single point: the start/stop point. Many part geometries, however, include a rastering infill, where the beads would overlap side-by-side. To make this extension, the response of the bead height to the mass rate input would need to be identified in x and y. A second avenue of furthering this work would be a multi-input, multi-output model and controller, where both the nozzle speed and some other parameter could be adjusted to achieve the desired output. For instance, the laser power and print speed could be simultaneously adjusted. When printing sharp corners, it may be difficult to control the height using print speed along, due to the large accelerations experienced at sharp corners. Although the literature agrees that height control by itself is not sufficient to maintain the desired layer thicknesses, it could be useful for supplementing the corrections performed via the nozzle speed.

REFERENCES

[1] Beaman, J., Bourell, D. L., Seepersad, C., and Kovar, D., 'Additive manufacturing review: Early past to current practice,' Journal of Manufacturing Science and Engineering, 2020, **142**(11), p. 110812

[2] Xiong, Y., Smugeresky, J. E., Ajdelsztajn, L., and Schoenung, J. M., 'Fabrication of wc–co cermets by laser engineered net shaping,' Materials Science and Engineering: A, 2008, **493**(1-2), pp. 261–266.

[3] Zhang, Y., Wu, L., Guo, X., Kane, S., Deng, Y., Jung, Y.-G., Lee, J.-H., andZhang, J., 'Additive manufacturing of metallic materials: a review,' Journal of Materials Engineering and Performance, 2018, **27**(1), pp. 1–13

[4] Strano, G., Hao, L., Everson, R. M., and Evans, K. E., 'Surface roughness analysis, modelling and prediction in selective laser melting,' Journal of Materials Processing Technology, 2013, **213**(4), pp. 589–597.

[5] Pinkerton, A., Wang, W., and Li, L., 'Component repair using laser direct metal deposition,' Proceedings of the Institution of Mechanical Engineers, Part B: Journal of Engineering Manufacture, 2008, **222**(7), pp. 827-836.

[6] Zhang, X., Li, W., and Liou, F., 'Damage detection and reconstruction algorithm in repairing compressor blade by direct metal deposition,' The International Journal of Advanced Manufacturing Technology, 2018, **95**(5),pp. 2393–2404.

[7] Hofmann, D. C., Kolodziejska, J., Roberts, S., Otis, R., Dillon, R. P., Suh,J.-O., Liu, Z.-K., and Borgonia, J.-P., 'Compositionally graded metals: A new frontier of additive manufacturing,' Journal of Materials Research, 2014, **29**(17), pp. 1899–1910

[8] Domack, M. and Baughman, J., 'Development of nickel-titanium graded composition components,' Rapid Prototyping Journal, 2005.

[9] Salehi, D. and Brandt, M., 'Melt pool temperature control using labview in nd: Yag laser blown powder cladding process,' The International Journal of Advanced Manufacturing Technology, 2006, **29**(3-4), pp. 273–278

[10] Tang, L. and Landers, R. G., 'Melt pool temperature control for laser metal deposition processes — part ii: layer-to-layer temperature control,' Journal of Manufacturing Science and Engineering, 2010, **132**(1)

[11] Bi, G., Schurmann, B., Gasser, A., Wissenbach, K., and Poprawe, R., 'Development and qualification of a novel laser-cladding head with integrated sensors,' International Journal of Machine Tools and Manufacture, 2007, **47**(3-4), pp. 555–561.

[12] Fathi, A., Khajepour, A., Toyserkani, E., and Durali, M., 'Clad height control in laser solid freeform fabrication using a feedforward pid controller,' The International Journal of Advanced Manufacturing Technology, 2007, **35**(3-4), pp. 280–292.

[13] Sammons, P. M., Bristow, D. A., and Landers, R. G., 'Two-dimensional modeling and system identification of the laser metal deposition process,' Journal of Dynamic Systems, Measurement, and Control, 2019, **141**(2).

[14] Sammons, P. M., Gegel, M. L., Bristow, D. A., and Landers, R. G., 'Repetitive process control of additive manufacturing with application to laser metal deposition,' IEEE Transactions on Control Systems Technology, 2018, **27**(2), pp. 566–575.

VITA

Michelle Lee Gegel earned a Bachelor of Science in Mechanical Engineering in 2015 from the Missouri University of Science and Technology (Missouri S&T). She received a Doctor of Philosophy in 2021, also in Mechanical Engineering from Missouri S&T. Prior to graduate school, she spent the summer of 2014 at Los Alamos National Laboratory as part of the Dynamic Summer School program. She was awarded the Chancellor's Distinguished Fellowship to begin a doctoral program at Missouri S&T and later received a GAANN Fellowship (Graduate Assistance in Areas of National Need). Michelle's doctoral research was a combination of control systems technology and additive manufacturing. As part of her graduate work, she built a metal deposition machine and implemented layer-to-layer feedback control on the process. She presented at the Solid Freeform Fabrication Symposium, the American Controls Conference and Dynamic Systems and Controls Conference. Lastly, she taught the lecture course entitled "Introduction to Automatic Control Systems" at Missouri S&T.